



TECHNISCHE  
UNIVERSITÄT  
WIEN



DIPLOMA THESIS

# Influence of B on the thermo-mechanical properties of reactively sputtered Ti-Si-N hard coatings

by

Lena Meiseleder, BSc BSc (WU)

Matr.Nr.: 1352728

Stella-Klein-Löw Weg 9/13

1020 Wien, Österreich

carried out for the purpose of obtaining the degree of Master of Science (MSc or Dipl.-Ing. or DI)  
under the supervision of

Projekttass. Dipl.-Ing. Dr.techn. Rainer Hahn

Ass. Prof. Dipl.-Ing. Dr.techn. Helmut Riedl-Tragenreif

E 308-01-2 - Institute of Materials Science and Technology  
Materials Science Division

submitted at

Technische Universität Wien

Getreidemarkt 9

1060 Wien, Österreich

Wien, 20<sup>th</sup> of May, 2023

---

*” Was wir wissen, ist ein Tropfen - was wir nicht wissen, ein Ozean”*

– Isaac Newton (1642-1727)

---

This work was supported by Boehlerit GmbH & Co.KG. within the framework of a project.

I confirm, that going to press of this thesis needs the confirmation of the examination committee.

*Affidavit:*

I declare in lieu of oath, that I wrote this thesis and performed the associated research myself, using only literature cited in this volume.

---

*Date*

---

*Signature*

---

# Acknowledgements

First of all, I want to thank the whole team for the warm welcome to the group and support from all sides, regardless of the topic and the constant availability for any questions. Greatest thanks go out to **Projektass. Dipl.-Ing. Dr.techn. Rainer Hahn** and **Assistant Prof. Dipl.-Ing. Dr.techn. Helmut Riedl-Tragenreif** for guiding me through this project with constant support and knowledge. I feel very lucky to have you as my supervisors! Furthermore, I want to thank **Dr. Arno Köpf** and **Dr. Margarethe Traxler** from Boehlerit GmbH & Co.KG. for their trust and giving me the opportunity to write my master thesis in cooperation with the company.

Big thanks to the (unofficial) Batcave chief **Univ. Ass. Dipl.-Ing. Balint Hajas** and **Univ.Ass.in Dipl.-Ing. Barbara Schmid**, for your constant help with any issues at Angie - no matter how banal these were. Also many thanks to **Univ.Ass.in Dipl.-Ing.Rebecca Janknecht**, **Senior Scientist Dipl.-Ing. Wojcik Tomasz** and **Projektass. Dipl.-Ing. Dr.techn. Lukas Zauner**, supporting me at certain measurements. Many thanks to my office colleagues **Emil, Philipp, Oskar** and **Christian** for the fun chats and open ear throughout these months and of course my initial office colleagues **Projektass.in Dipl.-Ing. Anna Hirle** and **Projektass.in Dipl.-Ing. Sophie Richter** for making me feel welcome from day one and always providing advice and support!

Not to forget the enthusiastic lecturers **Ahmed, Alex, Christoph, Helmut, Luki, Oliver, Rainer, Thomas** from the LU Surface Technology 2021W (despite certain COVID restrictions) triggering my interest for coatings and thus making a decisive contribution to write my thesis at the research group for Applied Surface and Coating Technology.

Finally, I want to thank my **family**, especially my mum (the definition of a **power-woman**) and **Alex** for your constant support and obviously my **friends** for both fun times but also understanding in busy phases throughout my studies!

---

# Contents

<b>Contents</b>	<b>v</b>
<b>List of Figures</b>	<b>viii</b>
<b>List of Tables</b>	<b>x</b>
<b>List of Equations</b>	<b>xi</b>
<b>List of Symbols &amp; Abbreviations</b>	<b>xi</b>
<b>Abstract</b>	<b>1</b>
<b>1 Introduction &amp; Motivation</b>	<b>3</b>
<b>2 Material System</b>	<b>5</b>
2.1 Ti-N . . . . .	6
2.2 Ti-Si-N . . . . .	7
2.2.1 TiN/Si <sub>3</sub> N <sub>4</sub> . . . . .	9
2.3 Ti-B-N . . . . .	10
2.4 Ti-Si-B-N . . . . .	11
<b>3 Physical Vapor Deposition</b>	<b>13</b>
3.1 Sputtering . . . . .	13
3.1.1 Direct current magnetron sputtering . . . . .	16

3.2	Microstructure . . . . .	16
<b>4</b>	<b>Characterization Methods</b>	<b>21</b>
4.1	Nanoindentation . . . . .	21
4.2	X-ray Diffraction . . . . .	24
4.3	X-ray Fluorescence Spectrometry . . . . .	26
4.4	Electron Microscopy . . . . .	27
4.4.1	Transmission Electron Microscope . . . . .	27
4.4.2	Scanning Electron Microscope . . . . .	28
4.4.3	Focused Ion Beam System . . . . .	29
4.5	Tribology . . . . .	30
4.5.1	Pin-on-disc . . . . .	30
4.5.2	Profilometer . . . . .	31
<b>5</b>	<b>Deposition Technique</b>	<b>33</b>
<b>6</b>	<b>Experimental Data and Discussion</b>	<b>36</b>
6.1	Preliminary study . . . . .	36
6.1.1	Structural Evolution and Morphology . . . . .	36
6.1.2	Mechanical properties . . . . .	44
6.1.3	Deposition rate . . . . .	47
6.2	Optimized parameter variations . . . . .	48
6.2.1	Elemental composition . . . . .	48
6.2.2	Structure and morphology . . . . .	51
6.2.3	Mechanical properties . . . . .	54
6.2.4	Tribological behavior . . . . .	56
6.2.5	Oxidation resistance . . . . .	59
<b>7</b>	<b>Conclusion</b>	<b>62</b>

**Bibliography**

**64**

## List of Figures

<b>Fig. 2.1</b>	Crystal structure of fcc TiN . . . . .	6
<b>Fig. 2.2</b>	Binary phase diagram for TiN at 1 bar . . . . .	7
<b>Fig. 2.3</b>	Ternary phase diagram of TiSiN at the isothermal section of 1273 K . . . . .	9
<b>Fig. 2.4</b>	Ternary phase diagram of TiBN . . . . .	11
<b>Fig. 3.1</b>	Sputtering process . . . . .	14
<b>Fig. 3.2</b>	Sputter yield as a function of the angle of incidence . . . . .	15
<b>Fig. 3.3</b>	Thin film growth models a) Frank van der Merwe layer by layer, b) Volmer Weber island growth, c) Stranksi-Krastanov combined mode . . . . .	17
<b>Fig. 3.4</b>	SZM for sputter-deposited films by Thornton . . . . .	19
<b>Fig. 3.5</b>	Structure Zone Diagram . . . . .	20
<b>Fig. 4.1</b>	Load-Displacement curve . . . . .	22
<b>Fig. 4.2</b>	Geometry of the Berkovich indenter with the contact area $A$ , face angle $\theta$ and distance $h_c$ . . . . .	22
<b>Fig. 4.3</b>	Interpretation of (a) elastic modulus and (b) hardness . . . . .	24
<b>Fig. 4.4</b>	Characteristic radiation . . . . .	25
<b>Fig. 4.5</b>	Geometrical configuration for derivation of Bragg's Law . . . . .	26
<b>Fig. 4.6</b>	Schematic illustration of (a) SEM and (b) TEM . . . . .	28
<b>Fig. 4.7</b>	Illustration of (a) elastically and (b) inelastically scattered electrons . . . . .	29
<b>Fig. 4.8</b>	Schematic illustration of pin-on-disc configuration . . . . .	31
<b>Fig. 4.9</b>	Confocal configuration . . . . .	32
<b>Fig. 6.1</b>	SEM cross-sections from Ti-Si-N coatings sputtered from Ti/TiSi <sub>2</sub> targets with various Si content (a) 10 at.% (b) 15 at.% (c) 20 at.% and (d) 25 at.% . . . . .	37
<b>Fig. 6.2</b>	X-ray Diffraction pattern for Ti-Si-N coatings with different bias potential using a Ti/TiSi <sub>2</sub> target with 15 at.% Si . . . . .	38
<b>Fig. 6.3</b>	SEM cross-section for Ti-Si-N coating sputtered from Ti/TiSi <sub>2</sub> target with 15 at.% Si and a substrate bias of -60 V . . . . .	39
<b>Fig. 6.4</b>	X-ray Diffraction pattern for Ti-Si-N coating with increasing cathode current . . . . .	40



<b>Fig. 6.5</b>	X-ray Diffraction pattern of Ti-Si-N thin films with different Si content within the targets . . . . .	41
<b>Fig. 6.6</b>	X-ray Diffraction Pattern for Ti-S-B-N coatings with different 2 <sup>nd</sup> TiB <sub>2</sub> cathode current . . . . .	43
<b>Fig. 6.7</b>	Hardness of Ti-Si-N coatings at different substrate bias . . . . .	44
<b>Fig. 6.8</b>	Influence of the Si content in the target on the (a) hardness and (b) Young's Modulus of Ti-Si-N coatings sputtered at different cathode current . . . . .	45
<b>Fig. 6.9</b>	Evolution of the (a) Hardness and (b) Young's Modulus for Ti-Si-B-N coatings as a function of the target current . . . . .	46
<b>Fig. 6.10</b>	Deposition rate as a function of the TiB <sub>2</sub> target current . . . . .	47
<b>Fig. 6.11</b>	Boron content in the coating as a function of the target current . . . . .	48
<b>Fig. 6.12</b>	Share of Si in the coating as a function of B . . . . .	49
<b>Fig. 6.13</b>	Ternary phase diagram for 10.75 at.% Si (blue) and 7.42 at.% Si (red) in the coating . . . . .	50
<b>Fig. 6.14</b>	SEM cross-sections for Ti-Si-B-N coatings co-sputtered from Ti/TiSi <sub>2</sub> with 15 at.% Si and a rising cathode current of (a) Ti <sub>0.84</sub> Si <sub>0.11</sub> B <sub>0.05</sub> N (b) Ti <sub>0.82</sub> Si <sub>0.11</sub> B <sub>0.07</sub> N and (c) Ti <sub>0.83</sub> Si <sub>0.10</sub> B <sub>0.07</sub> N for the TiB <sub>2</sub> target . . . . .	51
<b>Fig. 6.15</b>	X-ray patterns for Ti-Si(-B)-N coatings on (a) austenite and (b) WC-Co sorted by Ti/TiSi <sub>2</sub> target with increasing 2 <sup>nd</sup> TiB <sub>2</sub> target current . . . . .	52
<b>Fig. 6.16</b>	TEM bright field images and selected area electron diffraction (SAED) pattern for (a) Ti <sub>0.92</sub> Si <sub>0.08</sub> N, (b) Ti <sub>0.86</sub> Si <sub>0.07</sub> B <sub>0.07</sub> N and (c) Ti <sub>0.87</sub> Si <sub>0.07</sub> B <sub>0.06</sub> N coatings with increasing boron content, sputtered from Ti/TiSi <sub>2</sub> containing 10 at.% Si . . . . .	53
<b>Fig. 6.17</b>	Evolution of (a) hardness and (b) Young's modulus for Ti-Si-N coatings with increasing B content for selected Ti/TiSi <sub>2</sub> targets . . . . .	54
<b>Fig. 6.18</b>	H <sup>3</sup> /E <sup>2</sup> as a function over the boron content . . . . .	55
<b>Fig. 6.19</b>	Evolution of the coefficient of friction as a function of the sliding distance for (a) 10 at.% Si and (b) 15 at.% Si in the Ti/TiSi <sub>2</sub> target . . . . .	56
<b>Fig. 6.20</b>	COF as a function of the boron content . . . . .	57
<b>Fig. 6.21</b>	Young's modulus as a function of the COF for the two selected Ti/TiSi <sub>2</sub> targets . . . . .	58
<b>Fig. 6.22</b>	Evolution of the wear rate as a function of the boron content for the Ti/TiSi <sub>2</sub> target with 10 at.% Si . . . . .	59
<b>Fig. 6.23</b>	Evolution of the oxide layers over time for a) 10 at.% Si and b) 15 at.% Si within the Ti/TiSi <sub>2</sub> target . . . . .	60
<b>Fig. 6.24</b>	Oxide layer thickness for (a) Ti <sub>0.92</sub> Si <sub>0.08</sub> N and (b) Ti <sub>0.87</sub> Si <sub>0.07</sub> B <sub>0.06</sub> N coatings after 100 min at 800 °C . . . . .	61

---

## List of Tables

Table 5.1	Preliminary composition . . . . .	34
Table 5.2	Selected target composition . . . . .	35
Table 6.1	Elemental composition obtained from XRF results . . . . .	51

---

## List of Equations

(3.1) Momentum transfer for the sputtering process .....	14
(3.2) Surface and inter-facial free energies .....	17
(4.1) Contact area .....	22
(4.2) Elastic modulus defined by contact stiffness and contact area .....	22
(4.3) Combined elastic modulus $E^*$ .....	23
(4.4) Nanoindentation hardness .....	23
(4.5) Bragg's Law .....	25
(4.6) Constructive interference .....	25

---

## List of Symbols & Abbreviations

at.%	Atomic percent
BF	Bright field
DC	Direct current
fcc	Face-centered cubic
FIB	Focused ion beam
hcp	Hexagonal close-packed
kcps	Kilo counts per second
NaCl	Sodium chloride
PVD	Physical vapor deposition
SAED	Selected area electron diffraction
scm	Standard cubic centimetre per minute
SEM	Secondary electron microscope
SZM	Strucutre zone model
TEM	Transmission electron microscope
XRD	X-ray diffraction
XRF	X-ray fluorescence spectrometry

---

# Abstract

## Abstract

Hard Ti-Si-N coating materials are well-established in machining applications, due to their remarkable mechanical properties and oxidation stability. However, coatings for tribological applications require additional protection against wear and friction to extend the tool's lifecycle. Therefore, this work examines the influence of alloying boron to Ti-Si-N coatings to ameliorate the tribological behaviour, investigating the microstructure, mechanical and tribological properties as well as oxidation resistance. In a first step, reactive magnetron sputtering of Ti/TiSi<sub>2</sub> targets in mixed Ar/N<sub>2</sub> atmosphere (ratio 7/3) resulted in the formation of Ti-Si-N coatings. The silicon content in the target varied between 10 and 25 at.%, leading to a maximum in hardness of 35.7±0.96 GPa for estimated around 11 at.% Si within the coating. Higher Si contents lead to a decline in mechanical properties. To add boron, co-sputtering TiB<sub>2</sub> by varying the target current between 0.25 A and 0.75 A was conducted. This variation led to boron contents between 5.32 at.% and 7.01 at.% within the coatings. For Ti-Si-B-N coatings the hardness peaked at a boron content of 5.32 at.% sputtering the 10 at.% TiSi<sub>2</sub> target, reaching 36.5±1.49 GPa. A further addition of boron promotes the formation of amorphous BN phase regions accompanied by a decline in mechanical properties. The coating systems exhibit a super-hard nanocomposite structure with fcc-TiN nanocrystallites embedded in an amorphous Si<sub>3</sub>N<sub>4</sub> or BN matrix, respectively.

While the ternary system (Ti<sub>0.92</sub>Si<sub>0.08</sub>N) is more resistant against oxidation reaching a minimum oxide layer thickness of 319.5nm, Ti-Si-B-N coatings deposited from the Ti/TiSi<sub>2</sub> target with 10 at.% develop oxide layers between 433.7 and 507.8 nm (Ti<sub>0.86</sub>Si<sub>0.07</sub>B<sub>0.07</sub>N and Ti<sub>0.87</sub>Si<sub>0.08</sub>B<sub>0.05</sub>N) at 800 °C, after 100 min. On contrary, the coefficient of friction (COF) considerably decreases when alloying boron to the coatings decreasing from around 0.93 for the ternary system to 0.78 for Ti-Si-B-N films. The most severe drop in COF occurs between 5.3 at.% and 6.6 at.% boron within the coating, followed by a further slide decline.

## Kurzfassung

Die Kombination aus hervorragenden Härtewerten sowie ausgezeichneter Oxidationsbeständigkeit führt zum vielfachen Einsatz von Ti-Si-N Beschichtungen in der zerspannenden Industrie. Für Anwendungen im Bereich von verschleißfesten Werkzeugen, ist eine Verbesserung der tribologischen Eigenschaften jedoch unumgänglich. Speziell Legierungselemente wie Bor oder Molybdän die zu tribo-aktiven Layern führen, sind hier sehr interessant. Im Zuge dieser Arbeit wurde deshalb der Einfluss von Bor auf Ti-Si-N Schichten untersucht, um dadurch die tribologischen Eigenschaften des ternären Systems zu verbessern ohne maßgebliche Einbußen der mechanischen Merkmale zu erlangen.

In einem zweistufigen Ansatz wurden zuerst vier Ti/TiSi<sub>2</sub> Targets mit unterschiedlichem Siliziumgehalt zwischen 10 at.% und 25 at.% in einem reaktiven Gasgemisch aus Argon und Stickstoff reaktiv mittels Magnetron Sputtern abgeschieden. Eine maximale Härte von 35.7±0.96 GPa wurde für einen Silizium Gehalt von geschätzten 11 at.% (abgeschiedenen mit einem Ti/TiSi<sub>2</sub> Target mit 15 at.% Si) in der Schicht erzielt, gefolgt von einem Härteabfall bei steigendem Siliziumgehalt. Basierend auf der Auswertung der Strukturanalyse mittels XRD sowie den mechanischen Kennwerten, wurde das optimale Legierungsfenster für Ti/TiSi<sub>2</sub> Targets mit 10 at.% bis 15 at.% eingegrenzt.

Das Zulegieren von Bor erfolgte durch co-sputtern eines TiB<sub>2</sub> Targets unter einer Variation des konstanten Kathodenstroms von 0.25 A, 0.5 A und 0.75 A. Zusätzlich zur Phasenentwicklung und den mechanischen Merkmalen, wurden die Ti-Si-B-N Schichten auf deren tribologische Eigenschaften und Oxidationsbeständigkeit geprüft. Nach einem anfänglichen Härtemaximum von 36.5±1.49 GPa bei einem Borgehalt von 5.32 at.% führt ein steigender Borgehalt zu einem stetigen Abfall der mechanischen Kennwerte. Der Härteabfall sowie linear sinkende E-Modul sind auf einen steigenden Anteil einer amorphen BN Phase zurückzuführen. Dem gegenüber trägt die weiche BN-Phase signifikant zur Verbesserung des Reibkoeffizienten bei. Während ein Borgehalt von 5.32 at.% einen Reibkoeffizienten von 0.88 verzeichnet, sinkt dieser auf 0.78 bei 6.26 at.% Bor in der Ti-Si-B-N Schicht. Schichten in diesem Legierungsfenster weisen nanokristalline fcc-TiN Körner auf, umgeben von einer amorphen Si<sub>3</sub>N<sub>4</sub> beziehungsweise BN-Phasen. Die höhere Oxidationsbeständigkeit von Si<sub>3</sub>N<sub>4</sub> gegenüber BN führt dazu, dass das ternäre Schichtsystem (Ti<sub>0.92</sub>Si<sub>0.08</sub>N) eine minimale Oxiddicke von 319.5 nm und das quaternäre System Oxiddicken zwischen 433.7 und 507.8 nm aufweist (Ti<sub>0.86</sub>Si<sub>0.07</sub>B<sub>0.07</sub>N und Ti<sub>0.87</sub>Si<sub>0.08</sub>B<sub>0.05</sub>N) - Oxidations bei 800 °C nach 100 min.

---

# Introduction & Motivation

Draw peeling is a cutting method to manufacture wires, employing a one-feed motion to eliminate the entire circumferential surface of the cylindrical geometry [1]. However, the draw peeling dies are faced with severe issues of frequent tool wear, both economically and environmentally unsustainable. With increasing resource scarcity awareness, companies must spur research and development for existing resource-intensive processes. In this context, coatings not only affect the physical appearance of tools, as already discovered by the Egyptians covering wood with thin gold layers, but mainly act as a protective layer on surfaces [2]. Therefore, to counteract excessive tool wear, protective coatings can significantly extend the lifetime of tools while also improving the quality of the product.

Since each application differs in its performance requirements, no one-size-fits-all coating exists, requiring extensive research to find an appropriate coating composition. In the case of draw peeling, the coatings must exhibit relatively high hardness combined with an appropriate stiffness to improve the tribological behavior, reducing the abrasive wear in the contact area [3]. Besides, the cutting process is subject to high temperatures at the contact surface, requiring high oxidation stability.

Based on literature research, multicomponent nanostructured films can achieve superior coating properties by combining the different elemental properties [4, 5]. Shtansky et al. [3] suggest alloying transition metal coatings based on nitrides, carbides, and borides with elements like Si, Al, Cr, and others to enhance the coating properties. For example, Veprek [6] intensively investigated the concept of nanocomposite Ti-Si-N coatings, characterized by their high hardness and stability against oxidation due to the formation of  $\text{SiO}_2$ . Another nanocomposite coating attracting increasing attention is the TiBN system, characterized by enhanced wear resistance combined with considerable hardness, though at the expense of inferior oxidation stability, resulting from the soft amorphous BN phase in the film [7, 8]. Thus, the present work analyses the effect of alloying boron to Ti-Si-N coatings by reactive magnetron sputtering to achieve a coating that is both oxidation and wear-resistant. Ti-Si-B-N thin films have already been investigated by Fabrizi et al. [9], focusing on the thermal

stability and Shtansky et al. [3, 10] in several papers, but with high boron content leading to crystalline  $\text{TiB}_2$ .

This thesis aims to maintain the excellent mechanical properties and oxidation stability associated with Ti-Si-N films while improving the tribological properties by alloying only small amounts of boron to the coating system. Based on a two-step approach, physical vapor depositions of Ti/TiSi<sub>2</sub> targets with overall different silicon contents in nitrogen containing atmospheres are conducted to optimize the deposition parameters with respect to mechanical parameters and microstructural appearance. In the second step, a  $\text{TiB}_2$  target is co-sputtered at different target currents to examine the effect of increasing boron content on the coatings' phase evolution, hardness, tribology, and oxidation stability.



## Material System

The chemical element Titanium (Ti) is part of group IV of the periodic system and, therefore, belongs to the transition metals (TM), which are characterized by an unfilled or just-filled d-electron band [11]. The two characteristic temperatures for Ti are the melting point at 1670 °C and the allotropic phase transformation temperature at 882 °C [11, 12]. At 882 °C a phase transformation from hcp (hP2-Mg)  $\alpha$ -Ti to bcc (cI2-W)  $\beta$ -Ti takes place, though the density changes just slightly from 4.5 g per cubic centimeter to 4.4 g per cubic centimeter respectively [13]. Since Ti exhibits several advantageous properties, such as high-temperature stability, an attractive strength-to-weight ratio, and good corrosion resistance, the material is used for many applications, in the aerospace and chemical industry, for steam-turbine blades and implants in the medical field [11, 14].

However, substantial improvements regarding wear and oxidation resistance can be achieved by applying surface treatments to the material. The limited wear resistance is attributed to titanium's low  $c/a$  ratio in the hcp crystal structure, resulting in low shear strengths and a high coefficient of friction. While the oxidation resistance is excellent at lower temperatures, Ti quickly reacts with oxygen at temperatures above 430 °C, leading to embrittlement. [15] Therefore, nitriding Ti and Ti alloys is a popular surface treatment to improve the surface hardness, wear resistance, and oxidation resistance for applications under high friction and load [14, 15].

Interstitial elements, such as nitrogen, aluminum, and other non-transitional metals, belong to the group of  $\alpha$ -stabilizers for Ti. Compared to  $\beta$ -stabilizers, these elements do not affect the phase-transformation temperature or slightly increase it. While alloys with other TM ( $\beta$ -alloys) decrease the transformation temperature. [11]

Regarding the reactive sputtering process, which takes place in an Ar + N<sub>2</sub> gas mixture, the TiN alloy will be further investigated.

## 2.1 Ti-N

Alloying titanium with nitrogen (N) results in a face-centered-cubic (fcc) crystal structure (NaCl-type) and a lattice parameter of 4.240 Å at the stoichiometric composition [16]. As shown in Figure 2.1, the large red spheres demonstrate the metal atom (Ti), while the small green spheres are nitrogen positioned at the octahedral sites [17, 18]. Due to the occupation of interstitial sites in the metal lattice, TiN is also referred to as an interstitial alloy, crystallizing in a peritectic system (see Figure 2.2) [17]. For thin films, a columnar growth structure with a preferred (111) orientation is reported by Sundgren [16]. However, it should be noted that various PVD coating techniques exist with variable process parameters, thus, the characterization results can differ considerably [16].

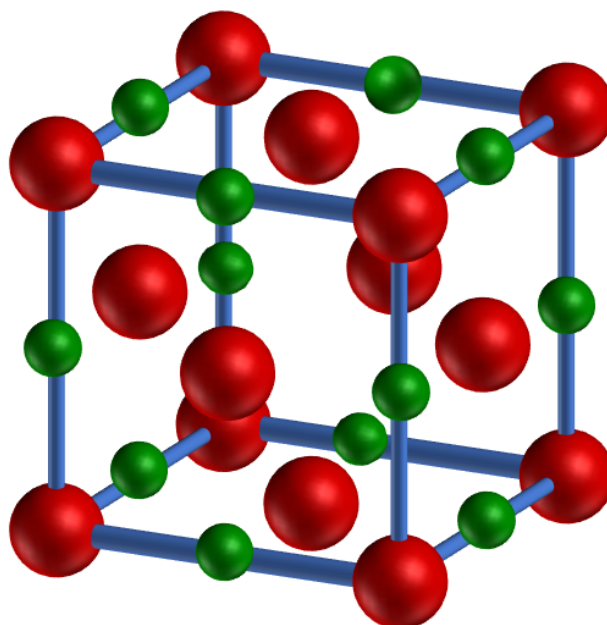


**Fig. 2.1:** Crystal structure of fcc TiN

The phase equilibria for TiN are intensively researched; thus, the binary phase diagram in Figure 2.2 illustrates the results from Khidirov [19] and Lengauer [20] combined by Okamoto [21]. As shown, titanium demonstrates a high solid solubility of nitrogen in  $\alpha$ -Ti, resulting in remarkable adherence to the substrate metal characterized by excellent hardness and shiny gold color. Its high stability over various compositions is due to its vacancy concentration.[12, 16]

Four different nitride compounds can be formed, namely  $\delta$ -TiN<sub>1-x</sub>,  $\epsilon$ -Ti<sub>2</sub>N,  $\eta$ -Ti<sub>3</sub>N<sub>2-x</sub>, and  $\zeta$ -Ti<sub>4</sub>N<sub>3-x</sub> [20, 22].

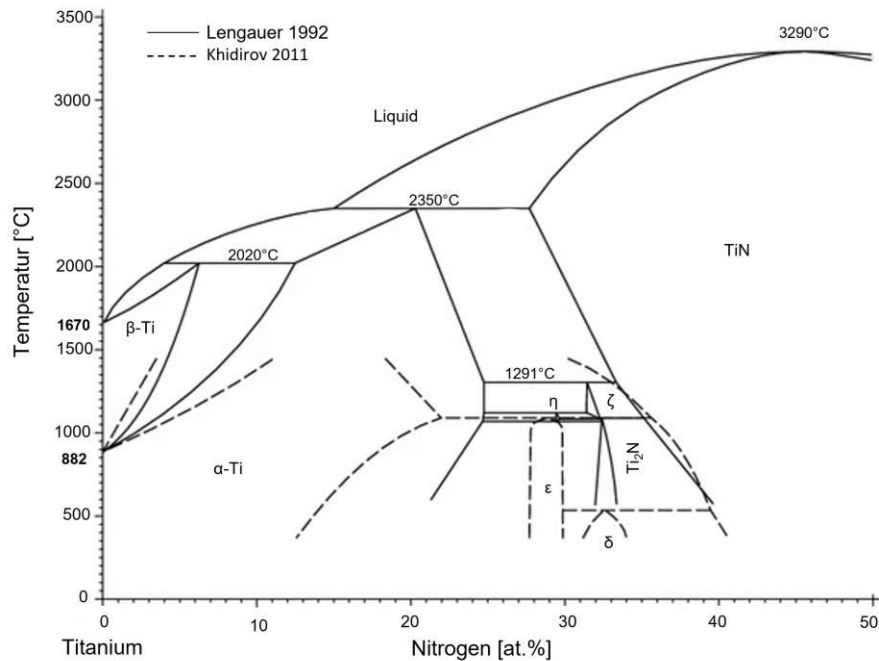


Fig. 2.2: Binary phase diagram for TiN at 1 bar, adapted from [21].

The compound material TiN exhibits an increased melting point of 3290 °C, indicating high cohesive strengths in the material [12, 17]. The highly directional coupling between Ti-3d orbitals and N-2p electrons results in a shear-resistant covalent bonding, significantly improving the hardness of the ceramic compound material [17, 23].

Due to the high hardness (Vickers microhardness of 2100 kg/mm<sup>2</sup>) and durability, TiN coatings are typically used for cutting tools. Furthermore, their good abrasion resistance and reduced friction make TiN an attractive protective coating material, especially for the semiconductor industry. [17, 18]

Overall, alloying Ti with N confirms a significant improvement in the physical properties as a coating material for cutting and forming tools, bearings, and more. However, exposed to higher temperatures (above 500 °C), the material system faces difficulties with its chemical stability. To overcome these drawbacks, multi-component materials such as Ti-Si-N significantly improve the stability at elevated temperatures and demonstrate rising hardness values. [24]

## 2.2 Ti-Si-N

Alloying an additional element to the binary TiN system ameliorates its physical properties resulting in either multilayers or nanocomposite hard coatings. As the name implies, a multilayer coating consists of a few different layers, such as a thin (0.05-1  $\mu$ m) Al<sub>2</sub>O<sub>3</sub>

layer between TiN layers, which is highly anisotropic. While nanocomposite hard coatings describe the simultaneous deposition, resulting in a nanocomposite material embedded in an amorphous matrix. This isotropic (random orientation) system requires that the two phases are entirely immiscible (thermodynamically segregated). The structural flexibility of the amorphous material allows for a tight encapsulation of the nanocrystalline material, thus, sharp interfaces arise and, consequently, increase the hardness of the coating. [25]

The ternary phase diagram Ti-Si-N (Figure 2.3) shows the existence of various two-phase regions. Worth mentioning is that the principle of mass conservation needs to be satisfied to allow for diffusion paths. [26]

Ma et al. [24] illustrate in their paper the development of the ternary phase diagram studied by Beyer and Sinclair [27] from 973 K to 1273 K, revised by Wakelkamp [28] at 1300 K, discovering the tie-line of TiN–TiSi<sub>2</sub> and Sambasivan and Petuskey [22] at 1273 K, introducing the compositional boundaries for the ternary solution Ti<sub>5</sub>Si<sub>3</sub>N<sub>x</sub>. While the phase diagrams mentioned above neglect an equilibrium between TiSi<sub>2</sub> and Si<sub>3</sub>N<sub>4</sub>, the papers by Paulasto et al. [26] and Rogl and Shuster [29] confirm a reaction of TiN and Si to form Si<sub>3</sub>N<sub>4</sub> or TiSi<sub>2</sub>, depending on the nitrogen activity. While the latter also supports the tie line of TiSi<sub>2</sub>–Si<sub>3</sub>N<sub>4</sub> [24].

Figure 2.3 visualizes the different compositional paths at 1000 °C (1273 K) based on the findings from Paulasto et al. [26]. The shaded areas demonstrate a two-phase equilibrium, while the open fields present the three-phase equilibrium. The phase diagram depicts the broad range of stoichiometry for TiN<sub>x</sub> ( $0.53 < x < 1.14$ ), which equilibrates with Si<sub>3</sub>N<sub>4</sub>, Si, TiSi<sub>2</sub>, TiSi, Ti<sub>5</sub>Si<sub>3</sub>N<sub>y</sub>, and Ti<sub>2</sub>N, depending on the nitrogen partial pressure. [22]

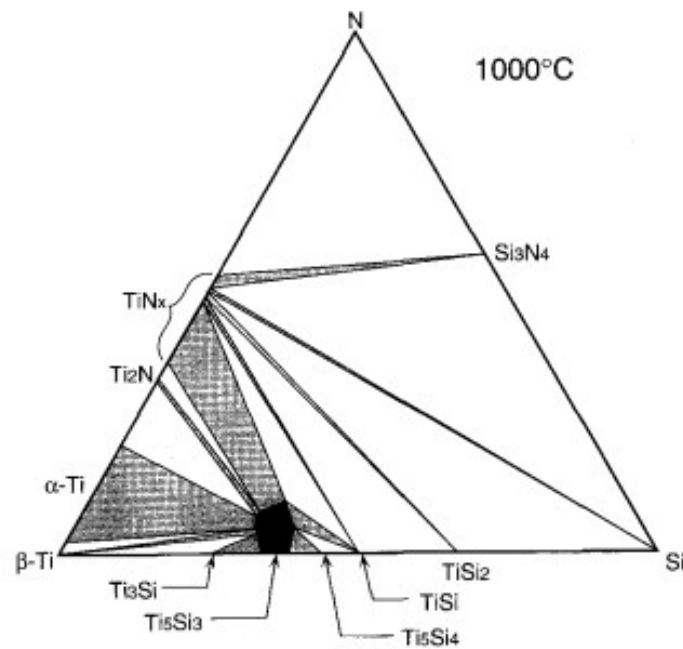


**Fig. 2.3:** Ternary phase diagram of TiSiN at the isothermal section of 1273 K, taken from [22].

### 2.2.1 TiN/Si<sub>3</sub>N<sub>4</sub>

The two-phase system TiN/Si<sub>3</sub>N<sub>4</sub> was first analyzed by Veprek et al. [30] and Shizhi et al. [31] using plasma-enhanced CVD, discovering the nc-TiN/a-Si<sub>3</sub>N<sub>4</sub> structure. To circumvent gas phase nucleation processes that impair the homogeneity of the film growth and prevent the potential incorporation of chlorine, Vaz et al. [32] and Diserens et al. [33] applied PVD techniques for the mentioned material system. During the process, a sufficiently high activity of nitrogen as reactive gas is necessary to discourage titanium silicide formation. [25]

An increase in hardness can usually be explained by one of the hardening processes associated with the movement of dislocations. For example, the Hall-Petch method relies on a decreased grain size, implying higher energy for the movement of dislocations. However, the nanocrystalline structure prevents the formation of any dislocations, as they cannot operate in such a small area of 2-5 nm [34, 35]. Thus, the nanocomposite structure's high hardness results from the interfaces' cohesive strength (preventing grain boundary sliding) and pseudoplastic deformation, acting as a strong, brittle material. In other words, the nanocrystals move towards each other, requiring more energy and enhancing hardness. [25, 35–37]

According to Veprek et al. [35], Ti-Si-N coatings with a Si content of 7-10 at.% exhibit the highest hardness values and demonstrate the smallest grain size, while Cheng et al. [38] argue that TiSi<sub>2</sub> phases form with increasing Si content, employing plasma-enhanced CVD technique.

Additionally, nc-TiN/a-Si<sub>3</sub>N<sub>4</sub> exhibits an enhanced oxidation resistance compared to TiN. At

the hardness maximum, corresponding to approximately 12 % a-Si<sub>3</sub>N<sub>4</sub>, the oxidation rate at 800 °C decreases about tenfold compared to TiN. Boosting the silicon nitride share would further strengthen the oxidation resistance but at the expense of a hardness loss. [25]

As reviewed by several studies, the improved oxidation resistance is either a result of forming a Si-rich diffusion barrier or can also be attributed to the strong and dense Si<sub>3</sub>N<sub>4</sub> interface that prevents oxygen diffusion along the grain boundaries [39, 40]. A growing share of Si in the coating leads to free Si diffusing towards the surface region, while the Si in the amorphous Si<sub>3</sub>N<sub>4</sub> compound is covalently bonded [31]. Consequently, SiO<sub>2</sub> is an efficient diffusion barrier against oxygen [39].

## 2.3 Ti-B-N

Similar morphological observations to nc-TiN/a-SiN<sub>x</sub> have been explored for Ti-B-N's ternary coating system. The addition of B to a TiN film results in a potential nanocomposite coating exhibiting fcc TiN crystals with preferred (111), (200), and (220) orientations surrounded by amorphous BN or TiB<sub>2</sub> phases. The boron-containing phases arise by precipitations at the grain boundaries, thus hindering grain growth and resulting in smaller grain sizes of around 5 nm [41]. The boron segregation at the boundaries allows for amorphous B-rich boundary phases with a remarkable cohesive strength [42]. Applying Monte Carlo simulations, calculations by Liu et al. [41] agree with their experimental observations, revealing a linear dependency of amorphous volume fraction and boron atomic concentration. Experiments conducted by Karvánková et al. [7] suggest that a boron content below 8 at.% leads to the formation of a BN phase, while a higher amount of B indicates the dominance of the TiB<sub>2</sub> phase. In terms of the microstructure, incorporating boron into transition metal nitrides, such as TiN or CrN, leads to grain refinement and the development of nanocomposite films, positively impacting the wear and mechanical properties [43].

Gissler [44] refers to the ternary phase diagram, first proposed by Nowotny [45] at 1500 °C. As shown in Figure 2.4 the simplified phase diagram points out two remarkable features: no ternary phases occur, only a modest boron solubility in titanium nitrides can be detected, and a negligible nitrogen solubility in TiB phases. The observed crystal structures for titanium borides are hexagonal AlB<sub>2</sub> type for TiB<sub>2</sub> and orthorhombic FeB type for TiB phases. [44]

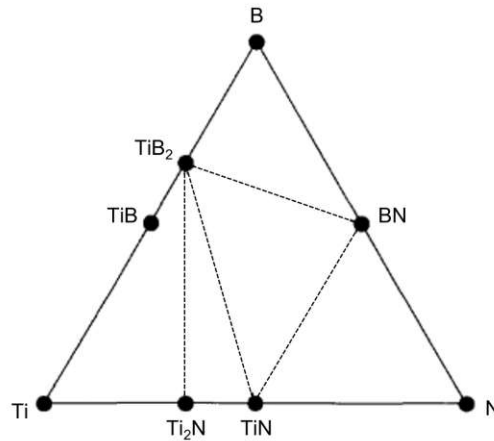


**Fig. 2.4:** Ternary phase diagram of TiBN, adapted from [44] after [45].

The ternary phase diagram, Figure 2.4, illustrates the vast flexibility of different phases, allowing to adapt the mechanical properties by adjusting the coating deposition conditions. For example, the compressive macro stress within the Ti-B films can be relaxed by increasing the substrate temperature  $T_s$ . [36, 46]

The extreme hardness for the ceramic  $TiB_2$  compound, with preferred (0001) orientation, can be attributed to the covalently bonded boron atoms within the Ti matrix, thus exhibiting twice the hardness of TiN and outperforming TiB [44, 46–48].

Overall, incorporating B into TiN films is widely acknowledged in literature to decrease the coefficient of friction (COF) and enhance the wear resistance of the tools [36].

## 2.4 Ti-Si-B-N

The addition of Boron to the ternary material system of Ti-Si-N has the same microstructural effect (a-BN) as Si (a- $Si_3N_4$ ), leading to a nano-crystalline to amorphous appearance through the formation of a-BN rich domains. In specific cases, this can positively influencing the thermo-mechanical properties of such nanostructured films. Regarding tribological behavior, Levashov et al. [5] refer to the ‘chameleon’ type of nanostructured films in their paper. These types of films possess a hard nitride or boride phase, responsible for a significant wear resistance under high load, and a soft a- $Si_3N_4$  or a-BN phase considerably decreases the COF [5].

The multicomponent coating Ti-Si-B-N crystallizes in a hexagonal close-packed (hcp)  $AlB_2$  structure, transforming to an fcc structure upon annealing [8]. Boron tends to deposit easily close to boundary regions or at surfaces due to low solubility in TiN. The resulting B-rich

disordered regions decrease the boundary mobility and favor the formation of  $\text{TiB}_2$ , in turn with a low solubility for N and disrupting the epitaxial growth by re-nucleation and leading to small crystallite sizes (2-4 nm). While TiB is characterized by an fcc phase,  $\text{TiB}_2$  crystallizes in an hcp structure, and like nitrogen, boron is positioned in the interstices of the (0001) close-packed Ti planes. Compared to the covalent component between Ti and N, the main covalent component for  $\text{TiB}_2$  is between the B atoms.  $\text{TiB}_2$  exhibits a melting point of 3225 °C and occurs in a narrow composition range of 65.6 to 66.7 at.% B. [37]

While the Ti-Si-N coatings exhibit a considerable increase in oxidation resistance, the nc-TiN/a-BN/a- $\text{Si}_3\text{N}_4$  structures indicate only a slight improvement in oxidation stability compared to TiN due to the low oxidation resistance of the soft BN phase [8].

Various papers confirm that the microhardness of the quaternary material system strongly depends on the stoichiometry. The maximum hardness values are measured for the strictly stoichiometric composition of  $\text{Ti}(\text{B},\text{N})_2$ . [5, 10]



---

# Physical Vapor Deposition

A physical or chemical process either achieves the deposition of thin films. As indicated by its name, physical vapor deposition (PVD) involves a physical transition from condensed to vaporized phase, unlike chemical vapor deposition (CVD), requiring a chemical reaction. Two main PVD methods can be distinguished depending on the physical technique for the phase transformation of the target material. While evaporation is characterized by heating the material (for example, by an electron beam or arc), thus transforming it to a liquid and then a gaseous phase, sputtering is a non-thermal vaporization process based on momentum transfer. [18, 49, 50]

Three main steps are involved in the PVD process. First, the vaporization of the target material, followed by the transportation through a plasma environment to the substrate, and finally, the condensation of the sputtered material at the substrate. The PVD process allows for the deposition of elements, alloys, and compounds by applying reactive deposition processes. [50]

## 3.1 Sputtering

Sputter deposition processes can be distinguished by various configurations, such as ion beam sputtering, magnetron sputtering, HIPPMMS, or radio frequency sputtering [50].

In most cases, the sputtering process occurs in a plasma ionizing the reactive gas, which is then accelerated toward the negative potential of the target [50]. Plasma describes the balanced state of ions and electrons, as well as neutrals, produced by direct current (DC), radio frequency (RF), or alternative current (AC). Applying a potential between the anode and cathode, a DC glow discharge can be generated, resulting from the deexcitation of excited Ar and the emission of photons. [18]

In general, the sputtering process can be classified as active or reactive. The sputtered target material forms a compound coating on the substrate by injecting a reactive gas, such as

oxygen or nitrogen, to the chamber. Worth mentioning, though, is that a hysteresis effect accompanies the flow of reactive gas. Once the share of reactive gas reaches a critical point, the deposition rate drops sharply. This behavior is attributable to target poisoning, describing the deposition of the compound material on the target, thus impeding the sputtering process. There exist several parameters influencing the hysteresis effect. Among them are the target material, the chosen reactive gas (for example,  $O_2$  is more reactive than  $N_2$ ), and the target-to-substrate distance. For example, reducing the target to substrate distance leads to a smaller hysteresis area. [18, 51]

The first step of the sputtering process is characterized by the momentum transfer describing the ion bombardment on the target surface. As illustrated in Figure 3.1, the working gas - in this case, Ar - is ionized by colliding with an electron ( $e^-$ ) and consequently accelerated towards the target surface (cathode). The energy transfer triggered by this impingement leads to the ejection of sputtered atoms, secondary electrons, ions, and neutrals. However, the impinging ion's threshold energy ( $E_{th}$ ) is required to initiate the sputtering process. [18]

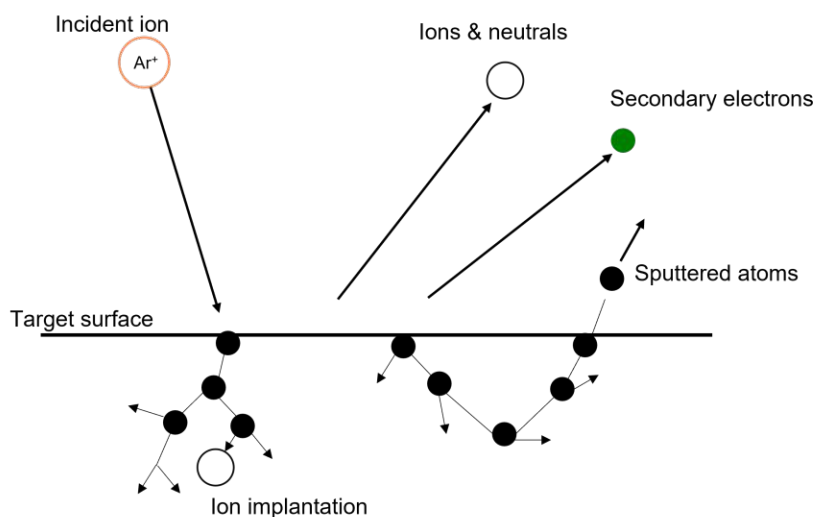


**Fig. 3.1:** Sputtering process, adapted from [18].

Over 95 % of the transferred energy is transformed into heat, demanding proper cooling for the target material to prevent damage. The momentum transfer is derived from the Law of the Conservation of Energy and the Conservation of Momentum by [50]

$$\frac{E_i}{E_t} = 4M_t M_i \frac{\cos\Theta}{(M_i M_t)^2} \quad (3.1)$$

In Equation 3.1, the index  $i$  refers to the incident particle, while  $t$  indicates the target particle. The energy given by  $E$  depends on the masses of the individual particles, given by  $M$  and the angle of incidence  $\Theta$ . By taking a closer look at Equation 3.1, it is evident that the

transferred energy is maximized at  $\Theta = 0$  ( $\cos 0 = 1$ ) and when the mass of the bombarding ion equals the mass of the sputtered atom ( $M_i = M_t$ ). [50]

In order to measure the efficiency of the sputtering process, the sputtering yield ( $Y$ ) is determined by the ratio of the number of ejected atoms to the number of impinging ions. The number of sputtered atoms depends on the chemical bonding of the target atoms, the ion energy, the masses of the involved atoms and ions, and the angle of incidence [50]. Sarkar [18] suggests that the sputter yield is higher for materials with a filled electronic d shell, such as copper, silver, and gold. A significantly enhanced sputter yield is also evident for increased ion energy. Furthermore, the sputter yield steadily increases with off-normal angles of incidence (also defined by  $1/\cos \Theta$ ) as depicted by the dotted line until reaching its maximum between  $60^\circ$  and  $80^\circ$ , followed by a sharp decline. [18]

Figure 3.2 illustrates the relative sputter yield for different metals (Ti, Al, Ta, and Ag) as a function of the angle of incidence  $\Theta$ . [18]

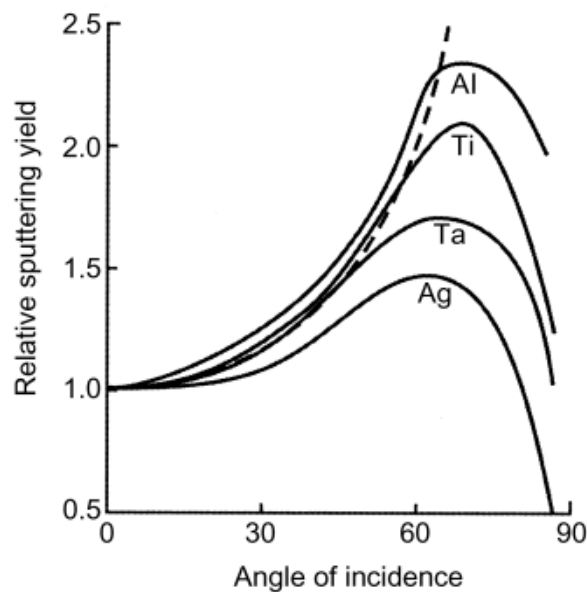


**Fig. 3.2:** Sputter yield as a function of the angle of incidence, taken from [18].

In the next step, the ejected atoms are transported through the plasma while experiencing collisions before reaching the substrate surface. The collision density heavily depends on the prevailing pressure in the chamber, which is inversely proportional to the mean free path describing the average distance between collisions [49, 50]. If the pressure is too high, multiple collisions decrease the ion energy and consequently reduce the deposition rate. Conversely,

low pressure is associated with fewer collisions and fewer Ar ions initiating the sputtering process on the target surface.

To ensure an improved sputtering efficiency while minimizing the energy loss by collisions, the emitted secondary electrons can be trapped close to the target surface by applying a magnetic field called magnetron sputtering [50].

### 3.1.1 Direct current magnetron sputtering

The self-sustaining effect of the glow discharge is based on the ongoing interaction between electrons and ions. However, the secondary electrons emitted by the target during ion impingement are accelerated away from the target, thus decreasing plasma density and sputter efficiency. In order to ameliorate the sputtering process, a magnetic field can be applied to trap the secondary electrons near the target surface, thus increasing the ionization close to the cathode. Thereby, the probability of collisions causing a loss in energy can be decreased, increasing the deposition rate while maintaining a lower potential on the target. [50]

Due to the helical path of the electrons, which is produced by the magnetic field ( $B$ ) perpendicular to the electric field ( $E$ ), the electrons generate an erosion track on the target material [18]. This leads to a non-uniform target utilization of only 10-30 % of the material before being recycled [50].

## 3.2 Microstructure

The final step in the PVD process describes the condensation of the sputtered material on the substrate, subsequent nucleation, and film growth. In the last step of PVD, the sticking coefficient is a relevant parameter, describing the ratio of condensing atoms to impinging atoms; since not all arriving atoms condense, some are directly reflected or reevaporate after some time. For example, the characteristic crystallographic planes of the material holding different surface-free energies are a primary factor for surface mobility. [15]

As a first step in atomistic film formation, adatoms condense on the substrate and form nuclei, exhibiting mainly three different nucleation forms (Figure 3.3). The Frank-Van der Merwe growth mode is characterized by layer-by-layer growth, implying that the arriving atoms are more strongly attracted to the substrate than each other. Conversely, if the adatoms are more strongly bonded to each other than the substrate, a three-dimensional island growth occurs, called Volmer-Weber mode. A combination of both growth models is represented by the Stranski-Krastanov mode, by preferring an initial layer growth followed by the formation of islands. [15, 18, 52]

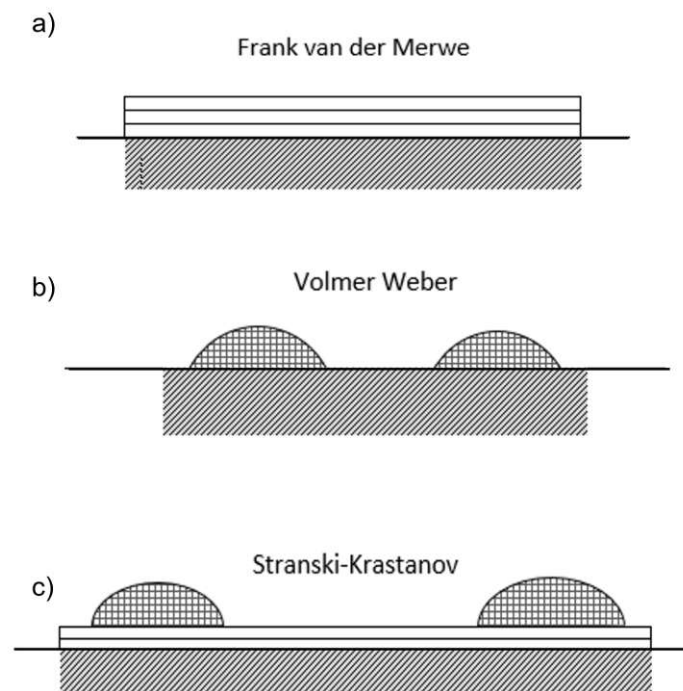


**Fig. 3.3:** Thin film growth models a) Frank van der Merwe layer by layer, b) Volmer Weber island growth, c) Stranski-Krastanov combined mode, adapted from [52].

These three growth modes can also be explained based on some thermodynamic considerations.

$$\gamma_{SV} \leq \gamma_{FS} + \gamma_{FV} \quad (3.2)$$

The Volmer-Weber growth prevails if Equation 3.2 is satisfied, claiming that the substrate-vapor free energy  $\gamma_{SV}$  is less than or equal to the combined free energies of the film-substrate  $\gamma_{FS}$  and film-vapor  $\gamma_{FV}$  interface. In other words, the energy can be minimized by the formation of islands that are characterized by a low surface-to-volume ratio. Conversely, by reversing the inequality of Equation 3.2, the Frank-van der Merwe mode is evident. [53]

### Evolution of the Structure Zone Models

With increasing film growth, various process parameters influence the resulting grain morphology, influencing the final film properties. The film morphology is typically described by a structure zone model (SZM) and was first developed by Movchan and Demchishin (1969) for vacuum-deposited films, later revised by Thornton [54] for sputter-deposited films [15], while the last modification was performed by Anders [55].

The later described zones are highly dependent on the surface roughness and the adatom mobility due to shadowing effects and surface diffusion. Inherently, the peaks of a rough surface are the first ones catching the impinging atoms (coating flux). Combined with low

surface mobility, the peaks grow faster than the valleys, resulting in the shadowing effect. [15]

Compared to the SZM proposed by Movchan and Demchishin, Thornton extended the model by the reactive gas pressure (Figure 3.4), drawing upon magnetron sputtering techniques [15]. While both models illustrate the morphology as a function of the homologous temperature  $T_h$ , defined by the ratio of substrate temperature  $T$  to the coating-material melting point  $T_m$  (both defined in Kelvin) [55].

Zone 1 is dominant for  $T/T_m < 0.3$ , showing a porous structure of sharp crystals separated by voids with a high dislocation density [54]. This structure evolves due to insufficient adatom surface diffusion, leading to the shadowing effect and continued nucleation of grains [15, 55]. An elevated working gas pressure expands Zone 1 to higher homologous temperatures due to gas adsorption and collisions on the surface, thus decreasing the kinetic energy [15]. With increasing  $T/T_m$ , Thornton [54] introduced the transition Zone T, defined by increased adatom mobility on the surface, thus overcoming the shadowing effect. The film is characterized by densely packed fibrous grains, especially at a lower pressure, due to highly energetic neutrals bombarding the peaks, subsequently partly filling the valleys [15].

With increasing  $T/T_m$ , the grain size increases, and the pressure influence decreases. Surface diffusion is dominant between a homologous temperature of 0.3 and 0.5, resulting in columnar grain growth separated by dense, intercrystallite boundaries. The coating appears smooth and mat, compared to brighter surfaces at  $T/T_m$  between 0.5 and 1, describing the final zone of the SZM. For zone 3, bulk diffusion prevails, allowing for recrystallization and grain growth, exhibiting an equiaxed growth. [54]

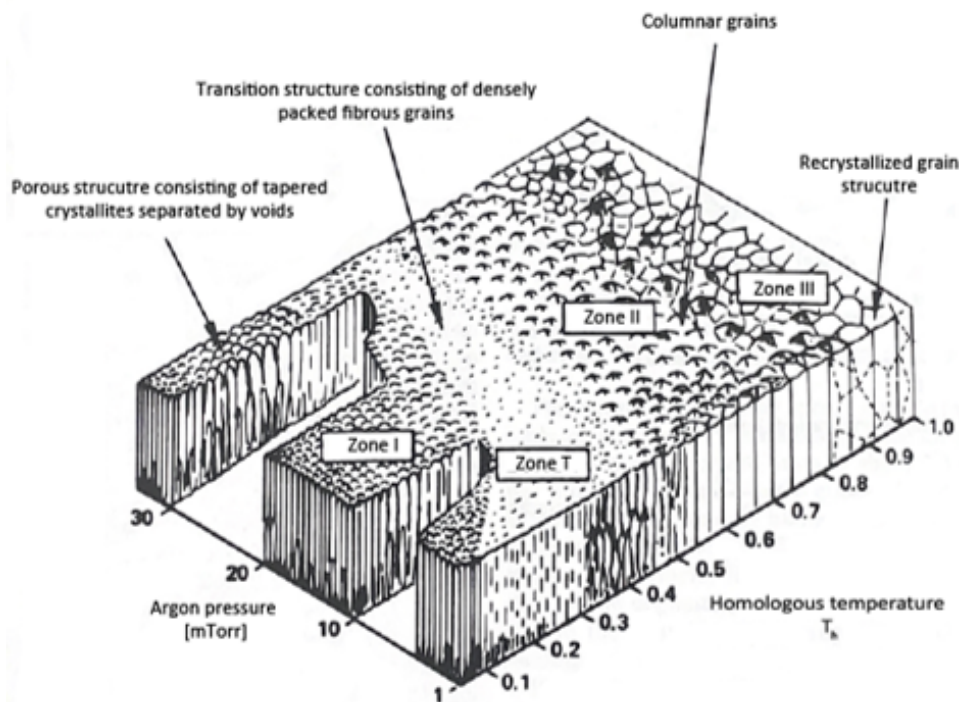


**Fig. 3.4:** SZM for sputter-deposited films by Thornton, adapted from [54].

Kunc et al. [46] applied the information from the SZM, suggesting increasing the ratio of  $T/T_m$  for  $\text{TiB}_2$  coatings to decrease intrinsic macro stress and improve the field of applications.

The constant technological development in deposition techniques led to the latest adaptations of Thornton's SZM by Anders in 2010, considering plasma-related deposition parameters (see Figure 3.5). Anders [55] mainly generalized the already existing axis of the diagram and introduced the net film thickness  $t^*$  to the z-axis, which even includes a negative thickness (red area) in case of ion etching. The homologous temperature was changed by the generalized temperature  $T^*$ , defined by the sum of the homologous temperature  $T_h$  and a temperature shift triggered by the potential energy of incoming particles (such as heat of sublimation)  $T_{pot}$ . While the kinetic energy of those particles, resulting in a displacement and heating effect, is illustrated by the logarithmic axis for the normalized energy  $E^*$ . [55]

Due to the mentioned heating effect, some areas in Figure 3.5 are not feasible, such as film growth at very low  $T^*$  and, at the same time, a high level of  $E^*$ , since the arriving particle energy significantly contributes to the heating of the coating. [55]

The main contribution of Anders' extended structure zone diagram is the inclusion of plasma and ion energy effects on film morphology.

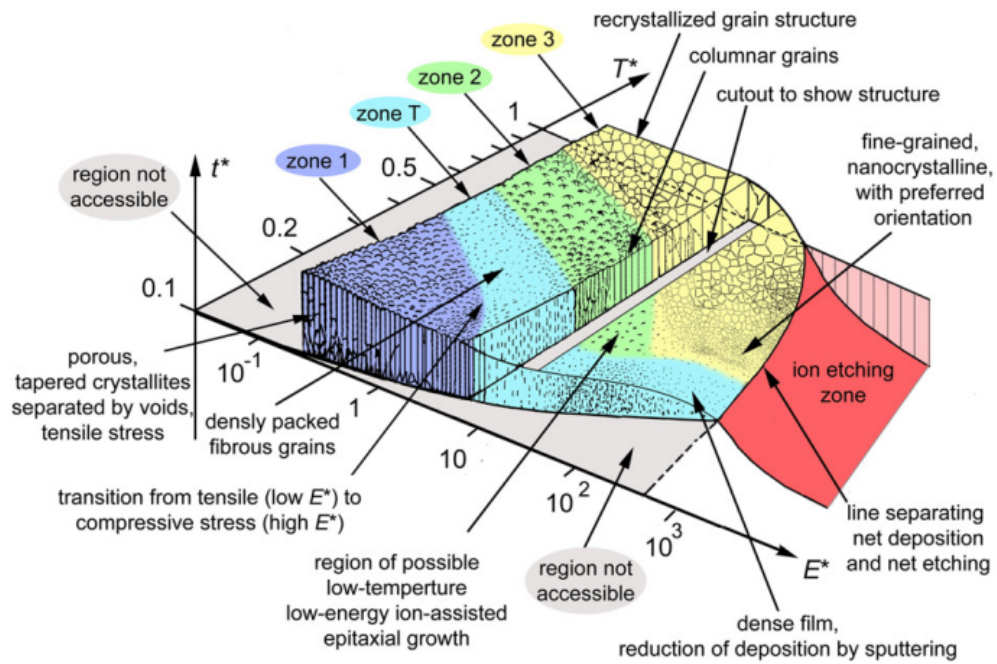


Fig. 3.5: Structure Zone Diagram, taken from [55].



---

# Characterization Methods

In order to analyze the mechanical and microstructural properties of the deposited thin films, different characterization techniques have been applied.

## 4.1 Nanoindentation

As the name of the method suggests, nanoindentation penetrates the specimen surface only some nanometres, thus exhibiting a suitable technique for thin films.

The applied load of the indenter, together with its recorded penetration, the depth is measured in order to calculate the area of contact and thus characterize the mechanical properties, such as hardness and elastic modulus of the corresponding specimen. The three-sided Berkovich indenter, usually made from diamond, is the most commonly used for nanoindentation testing. Compared to the four-sided Vickers indenter, which is often used in microhardness testing, the three faces of the Berkovich indenter simplify the grinding towards a single point, while the tip of Vickers tends to form an unwanted line of conjunction. [56]

Figure 4.1 illustrates a typical load and displacement curve arising from a nanoindentation measurement. The specimen is first elastically deformed upon loading and reaches a fully developed plastic zone at the maximum load  $P_{max}$  and depth  $h_{max}$ . In comparison, the unloading of the indenter is characterized by some elastic recovery of the specimen, subsequently, the area between the two slopes describes the energy loss due to plastic deformation. [56]

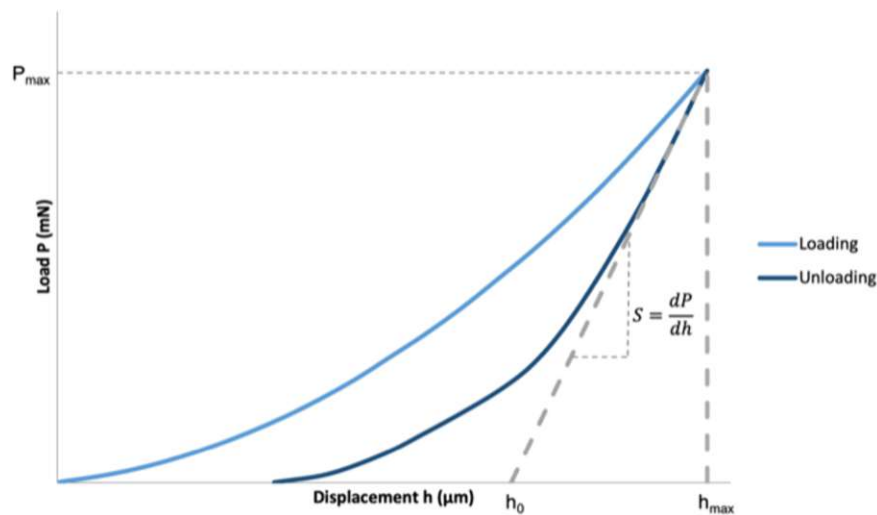


**Fig. 4.1:** Load-Displacement curve, adapted from [57].

For the calculation of the elastic modulus, the unloading data is required. As shown in Equation 4.2, the contact stiffness,  $\frac{dP}{dh}$  defined by the derivative of the load with respect to the displacement, together with the contact area  $A$ , is necessary to determine the combined elastic modulus  $E^*$  of the specimen material and the substrate. Equation 4.1 requires the contact depth  $h_c$ , which defines the distance between the circle of contact and the tip of the indenter, as shown in Figure 4.2, illustrating the geometry of the Berkovich indenter, the contact area  $A$ , face angle  $\theta$ , and distance  $h_c$ . [15, 56, 57]

$$A = 24.5h_c^2 \quad (4.1)$$

$$E^* = \frac{1}{\beta} \frac{dP}{dh} \frac{1}{2} \frac{\pi}{A} \quad (4.2)$$

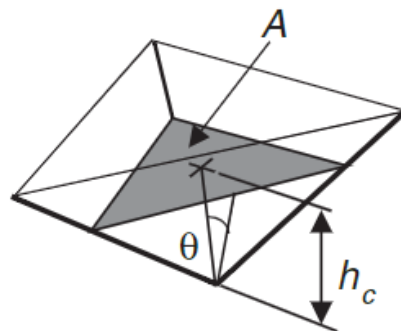


**Fig. 4.2:** Geometry of the Berkovich indenter with the contact area  $A$ , face angle  $\theta$  and distance  $h_c$ , taken from [56].

Since the indenter is made from diamond, the combined elastic modulus is mainly dominated by the specimen's elastic modulus  $E$ . However, Equation 4.3 shows the correlation between  $E^*$ ,  $E$ , and the elastic modulus of the indenter  $E'$ , as well as the corresponding Poisson ratios  $\nu$  and  $\nu'$ . Moreover, as a rule of thumb, the indentation depth should not exceed 10 % of the film thickness to minimize substrate influences. On the other hand, the hardness can be calculated by dividing the maximum load  $P_{max}$  by the contact area  $A$  (Equation 4.4). [15, 56, 57]

$$\frac{1}{E^*} = \frac{(1 - \nu^2)}{E} + \frac{(1 - \nu'^2)}{E'} \quad (4.3)$$

$$H = \frac{P_{max}}{A} \quad (4.4)$$

Nevertheless, specific corrections need to be applied to derive the correct results. Among them is the initial penetration, which shifts the load-displacement curve to the right by adopting the contact point and the area function, considering geometric deviations of the indenter tip due to manufacturing or use. Other but more complex corrections are required for material issues, such as piling-up leading to the support of the indenter, thus less penetration and an overestimated value for  $E$  and  $H$ . [56]

For a correct interpretation of the measured data, the following methods have been applied: In order to reduce the effect of the substrate modulus, an extrapolation technique was applied. This means that the measured data points for the elastic modulus are plotted as a function of the penetration depth and fitted by a curve. Since the lower penetration depth values better represent the film properties, without any substrate influence, the curve is extrapolated back to zero penetration, intersecting the y-axis to obtain the best estimate of the film modulus  $E$  (see Figure 4.3a). A similar approach was chosen for the hardness, plotting the measured data points against the depth; three stages can be detected. The initial rise can be ascribed to the elastic contact due to the round indenter tip, followed by a plateau indicating the fully developed plastic zone, and finally, a fall-off or increase resulting from the substrate properties at higher penetration depths. [56]

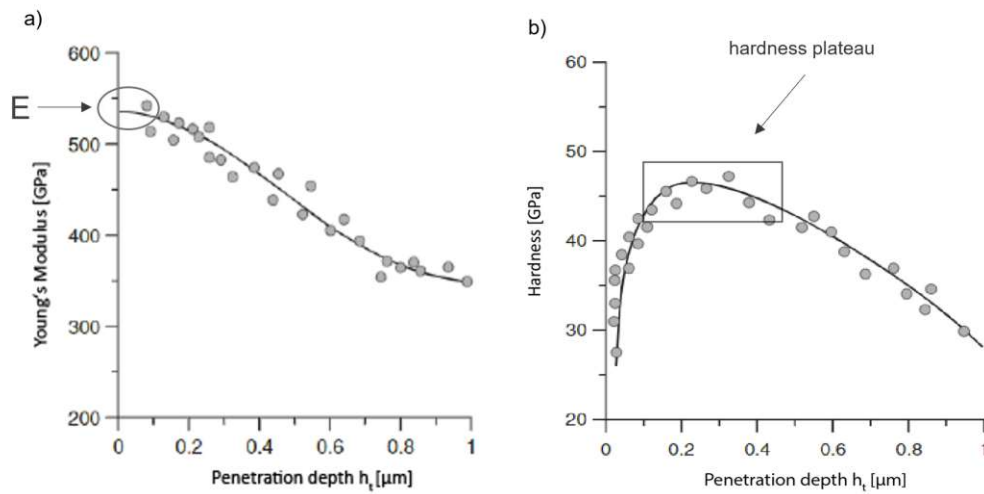


**Fig. 4.3:** Interpretation of (a) elastic modulus and (b) hardness, adapted from [56].

A UMIS Nanoindentation system performed the nanoindentation tests with a Berkovich diamond tip on austenite substrates and WC-Co cutting inserts. For the results, a map file was used, programmed with 31 indentation steps, and an initial load of 45 mN gradually decreasing until reaching a final load of 3 mN.

## 4.2 X-ray Diffraction

X-ray diffraction (XRD) is a non-destructive method to derive microstructural information, such as phase composition, structure, and preferred crystal orientations (texture) of powder as well as solid and even liquid samples [58–60]. This analytical method is based on the systematic and periodic arrangement of atoms in elements and compounds, defined by the unit cell and the spacing described by the specific lattice parameters of the crystal structures [15, 61].

The basic principle behind XRD is a monochromatic X-ray beam that impinges the sample surface and produces constructive interference, thus generating a diffraction signal that is collected and processed by an X-ray detector [15].

In a cathode ray tube, electrons are accelerated towards a target (the anode), resulting in the ejection of electrons (Figure 4.4). Based on the Bohr model, the transition from a higher shell (e.g., L-shell) electron to the void in the lower shell (K-shell), characterized by lower energy, releases energy and thus leads to characteristic radiation. In the case of Cu- $K\alpha$  radiation, the resulting X-rays exhibit a wavelength ( $\lambda$ ) of 1.5418 Å, which is inversely proportional to the energy. Nevertheless, this process is relatively inefficient, mainly converting the kinetic

energy into heat, and only a tiny fraction results in X-rays, thus requiring an effective cooling system for the anode. [58, 59]

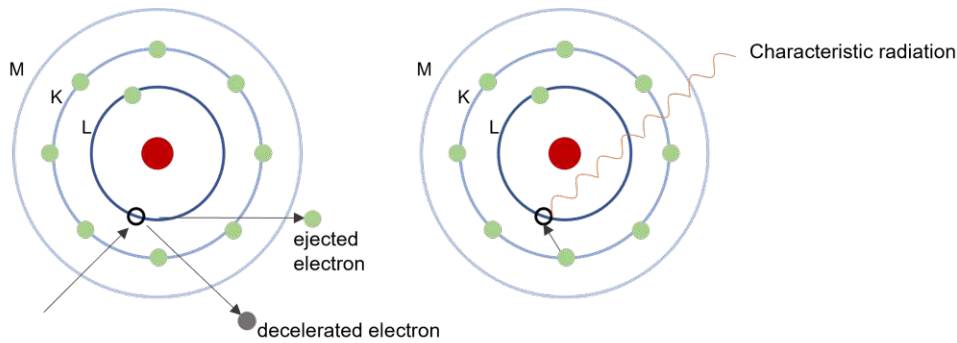


Fig. 4.4: Characteristic radiation adapted from [58].

In principle, to obtain a signal at the detector, Bragg's Law has to be satisfied:

$$2d_{hkl} \sin \theta = n\lambda \quad (4.5)$$

where  $d_{hkl}$  defines the interplanar spacing with the corresponding Miller indices  $hkl$  for the different crystal systems,  $\theta$  describes the diffraction angle,  $\lambda$  as already mentioned, is the characteristic wavelength, and the integer  $n$  refers to the reflection order [59, 60].

From a geometrical point of view, Equation 4.5 can be derived with the help of Figure 4.5. The illustration demonstrates the arriving radiation on the lattice planes (impinging on the atoms M and N), characterized by their specific crystal spacing  $d$  and then diffracted at the same incident angle  $\theta$ . However, Bragg's Law is based on the assumption of constructive interference, described by the elastic scattering process, which only takes place if the phase shift of the reflected radiation is a multiple of the wavelength: [58, 59]

$$n\lambda = PN + NQ \quad (4.6)$$

Considering the following mathematical relationships from Figure 4.5:

$$\sin \theta = \frac{PN}{MN} = \frac{NQ}{MN}$$

$$d_{hkl} = MN$$

Equation 4.6 can be rewritten as Bragg equation.

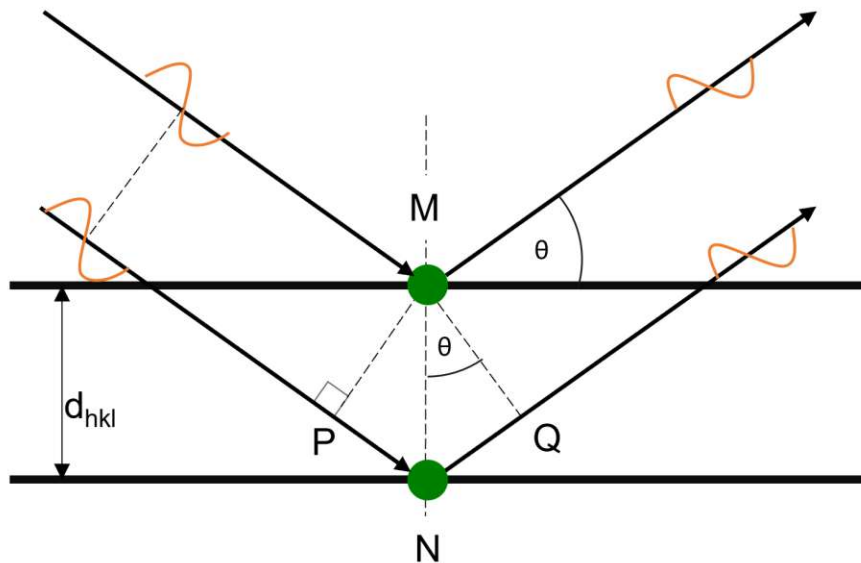


**Fig. 4.5:** Geometrical configuration for derivation of Bragg's Law, adapted from [62].

The resulting intensity of the produced diffraction peaks is plotted as a function of the diffraction angle, which can then be compared to reference patterns [15, 58]. Deviations from these patterns can have various reasons. For example, residual stress within coatings tends to slightly shift the position of the peaks to higher angles [15], whereas a broadening of the peaks implies a diminution of the grains [60]. Overall, the position of the diffraction maxima provides information about the size and shape of the unit cell, while the corresponding width indicates the size, orientation, and strain in grains, and the intensity suggests the preferred growth orientation [15].

The XRD analysis for the present work was performed on a Philips XPERT diffractometer operating the Bragg Brentano configuration and Cu-K $\alpha$  radiation, analyzing the austenite and WC-Co substrates.

## 4.3 X-ray Fluorescence Spectrometry

X-ray fluorescence (XRF) spectrometry is a rapid, accurate, and non-destructive quantitative method to determine the elemental composition or thickness of the specimen by measuring the X-ray emission wavelength or energy. Thus, categorizing the available spectrometers into two groups, wavelength dispersive and energy dispersive instruments. In the latter case, a high-resolution Si(Li) solid-state detector is used to measure lower-energy X-rays, and in both cases, an X-ray tube is employed as the excitation source. Software systems do the following data collection and processing. However, to excite a specific characteristic line, the source must be operated with a voltage  $V_0$  significantly above the critical excitation potential

$V_c$  of the element. The detector then converts the thereby emitted photons to counts per second. [63]

As explained in Chapter 4.2, the irradiation of high-energy X-ray photons ejects electrons from the atoms, thus, creating vacancies within the atom shells. These voids are filled with outer shell electrons, characterized by higher energy, resulting in energy emission (so-called excitation energy), referred to as fluorescence. Each emission line can be assigned unambiguously to an element. [64, 65]

The coated WC-Co substrates have been placed in the XRF analyzer. In order to determine the chemical composition, a TiSiB reference data set was used to design a calibration curve showing the kilo counts per second (kcps) as a function of the wt.% for each element and subsequently converted the obtained values to at.%; this procedure is based on the matrix effect, describing the correlation between X-ray intensity and elemental concentration [63].

## 4.4 Electron Microscopy

While light beams in optical microscopy are limited to wavelengths in hundreds of nanometers, electron beams enable image resolution in the micro to the nanometer range. Thus, transmission and scanning electron microscopy help to analyze sample specimens' morphology, crystal and grain structure, and porosity. [66, 67]

### 4.4.1 Transmission Electron Microscope

Transmission electron microscopy (TEM) explores the ultrastructure of thin specimens, providing information about the grains, their dislocations, and the slight angle boundary distribution by recording an image with magnifications in the range of  $10^3$ - $10^6$ . [68, 69] Electrons produced and accelerated by an electron gun penetrate a thin sample and are collected by a detector parallel to the specimen to produce a high-magnification image on a fluorescent screen. Particularly noteworthy for this technique is that the energy of the electrons is in the range of 80-300 keV, and the specimen is extremely thin (typically around 100 nm) to ensure electron transmission rather than scattering or absorption. [69, 70]

The electron gun consists of a cathode acting as the electron source and an electric field accelerating the electrons parallel to the optic axis. The electric field is generated by a potential difference between the cathode and an anode with a central hole, creating a stationary electron beam with a diameter of 1  $\mu$ m or more. Requiring a fragile specimen limited the field of applications, consequently leading to the development of scanning electron microscopy to investigate bulk specimens. [69]

The coated austenite specimens have been covered with an ultrathin tungsten layer to create the thin samples using the Thermo Fisher Scios II FIB system. The subsequent TEM analysis

was operated on a TECNAI F20 with a field emission gun to create bright field and dark field images.

#### 4.4.2 Scanning Electron Microscope

While TEM analyses the internal microstructure of the specimen, scanning electron microscopy (SEM) primarily investigates the material surface [70]. The main differences can be detected immediately in Figure 4.6. Firstly, the electron beam referring to SEM is scattered by the bulk specimen, thus simplifying the specimen preparation, and secondly, the respective electron beam is sharply focused, scanning the probe in two directions.

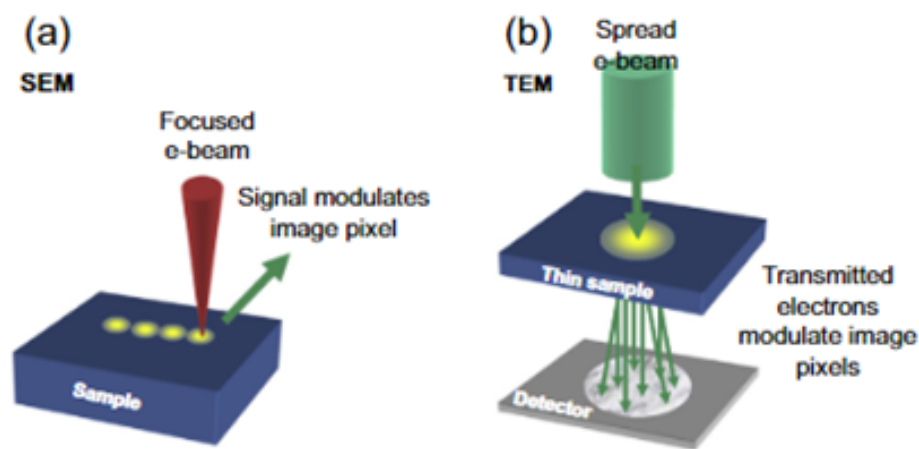


**Fig. 4.6:** Schematic illustration of (a) SEM and (b) TEM, taken from [70].

Similarly to TEM, the method consists of four components: the electron column, a specimen chamber, the vacuum pumping system (generating a pressure of around  $1.3 \cdot 10^{-4}$  Pa using a turbomolecular pump), and an imaging system [65]. The process involves a highly focused electron beam, impinging on a specimen surface, and collecting the emitted electron signals by a detector to produce an image [70].

In comparison to TEM, the electron source can be thermionic, such as a tungsten or  $\text{LaB}_6$  (lanthanum hexaboride) filament or a Schottky emitter, which is subsequently focused by two magnetic lenses to typically 10 nm in diameter on the specimen. The accelerated electrons indicate a lower kinetic energy than for a TEM, thus the electron gun is smaller requiring less insulation. [67, 69, 71]

In order to scan the specimen in a raster-like manner, scan coils (as a last step in the electron column) deflect the beam from the central optic axis in two perpendicular directions (x and y). The incident beam, also called electron probe exhibits an energy of 1-30 keV and a beam current of 1 nA. [69, 71]

When the primary beam impinges on the surface various physical processes or so-called “scattering events” occur. On the one hand, inelastic scattering takes place if the primary



electron interacts with the atomic electrons, resulting in secondary electrons (SE) (Figure 4.7b). In this process the electron beam ejects a weakly bound outer-shell (valence) electron hence, indicating a significant energy loss. On the other hand, elastic scattering results in backscattered electrons (BSE), which preserve a considerable amount of incident energy (typically 50 % or even more). In this case the electron beam electrostatically interacts with the atomic nuclei, thus deviating from its previous path (Figure 4.7a). [69, 71]

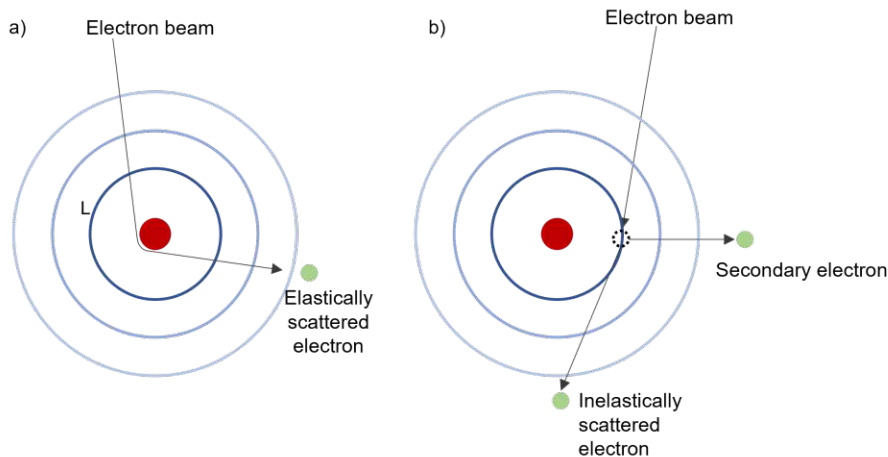


**Fig. 4.7:** Illustration of (a) elastically and (b) inelastically scattered electrons, adapted from [72].

In order to interpret the resulting signals, different detectors need to be applied. While, as already mentioned, SE leave the specimen usually with less than 10 eV, they require a rise of kinetic energy to create scintillation. The Everhart-Thornley detector is commonly used for interpreting SE signals and is supplied by a Faraday cage to accelerate the electrons, applying a positive potential. As a result, the SE detector mainly illustrates the specimen's topography. Compared to SE, BSE indicate a high kinetic energy and therefore are directly detected by a Robinson (passive) detector, providing information about the crystallography and orientation. [69, 71]

The SEM pictures have been created at a Zeiss Sigma 500 VP equipped with a field emission gun and the Inlens Duo detector, examining the cross-sections of the silicon substrates. The electron high tension was operated at 3.00 kV, and the images were taken at a magnification of 20.00 kX.

#### 4.4.3 Focused Ion Beam System

Another source of secondary electron generation, but one that damages the sample, is an ion beam produced by an LMIS (Ga) or plasma source, hence referred to as ion-induced secondary electrons (iSE). Focused ion beam (FIB) systems are mostly installed as a two-column system with an SEM column, requiring the same Everhart-Thornley detector as explained above.

Compared to SEM, the yield of secondary electrons per incident particle generated by an ion beam is higher and free of BSE, subsequently, FIB images show a more excellent grain contrast. The image resolution depends, on the one hand, on the beam size generated by the ion columns (increasing with higher current) but especially on the milling rate of the sample, demonstrating an improved image resolution for materials with a slow sputtering rate. [71] FIB analyses have been conducted on a Thermo Fisher Scios II, equipped with  $\text{Ga}^+$  ions to determine the oxide layer thickness obtained at  $800^\circ\text{C}$  annealing temperature. The sapphire substrates have been placed in the heated furnace for 10, 25, and 100 min. Since sapphire is not conductive, the samples have been coated with very thin layers (4 nm) of gold-palladium to produce conductivity for imaging. The images have been magnified at 60.00 kX, accelerating the electrons at a high voltage of 10.00 kV.

## 4.5 Tribology

To investigate the coating's tribological properties, a pin-on-disc test was performed, followed by a profilometer analysis for the wear rate. However, as stated in various papers, the uncertainty of these parameters has to be considered, indicating deviating friction properties even within existing literature [73]. Nevertheless, the wear rate is a significant parameter to measure the lifetime of the coating-substrate system [74].

### 4.5.1 Pin-on-disc

The experimental measurement consists of a stationary steel ball pressed against a rotating disc with a predetermined speed. As the name implies, the loading arm is loaded with appropriate weight and balanced by the counterweight (see Figure 4.8). The coefficient of friction (COF) is determined with a sensor by measuring the tangential force needed to retain the ball. The resulting test data provides a steady COF as a function of distance (after a run-in period) until the coating fails, leading to a rise or drop in the signal. [74, 75]

Depending on the material application, a higher load with a smaller rotating radius is chosen to simulate harsh conditions, while a lower load with a larger contact geometry records the evolution of the COF over time. Tribometer tests can also be performed at high temperatures by surrounding the sample with an oven. These tests can reveal the influence of hard oxide layers developed at higher temperatures, leading to a decrease in wear. High-temperature tests thus provide relevant information for high-temperature cutting applications. [74]

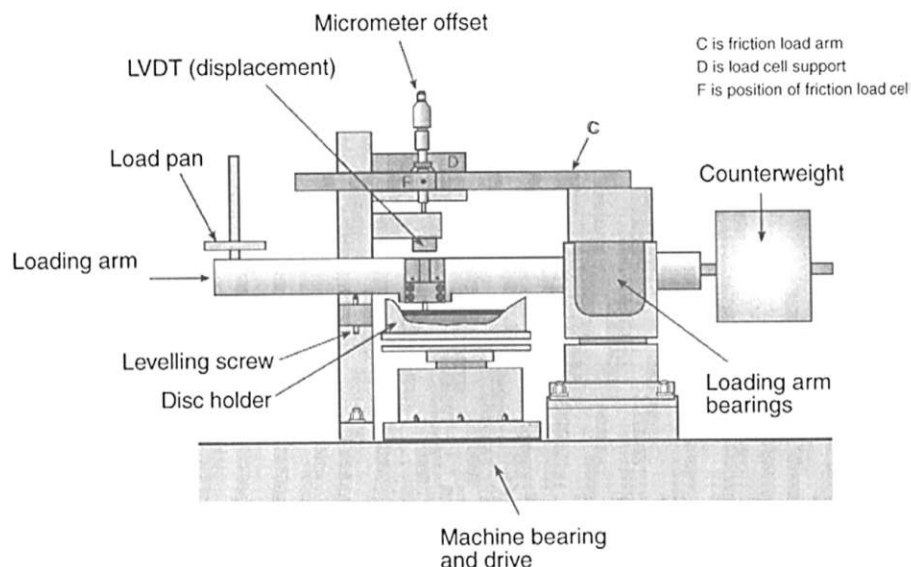


**Fig. 4.8:** Schematic illustration of pin-on-disc configuration, taken from [75].

The tests were carried out at Nanovea – T50 at room temperature with a 100Cr6 steel ball (diameter 6 mm) acting as a counterpart. For the measurement, the applied load was 1N, and the sliding distance was set to 35 m to obtain the COF and 200 m to receive more precise results for the wear rate calculation. To prevent unintended friction by impurities on the surface, the WC-Co discs have been cleaned with isopropanol.

## 4.5.2 Profilometer

Subsequently, the samples are examined by a profilometer to analyze the profile of the created wear track and obtain a value for the wear rate (usually indicated in  $\text{mm}^3/\text{Nm}$ ). For this method, the worn sectional area is calculated [ $\text{mm}^2$ ] multiplied by the diameter [m], leading to a volume of the amount removed, and finally divided by the applied load (1 N) and sliding distance (200 m) to indicate the wear rate.

The non-contact PS50 profilometer by Nanovea employs the chromatic confocal technique for surface topography analysis. Based on a lateral single-point scanning system, the chromatic confocal probe measures the light intensity and thus extracts the height of the surface. During the measurement, the microscope is static, and only the stage on which the workpiece is placed moves in a predefined x and y direction. Figure 4.9 demonstrates a classical confocal configuration. Worth mentioning is that the distance between the light source and the substrate surface (1-6) is equivalent to the path between the substrate surface and the photodetector (6-3-2). In order to obtain a signal at the detector, the surface needs to be in focus, or the focal point must lie precisely on the surface, consequently reflecting the incoming light through a pinhole. Otherwise, the light intensity is close to zero, not detected by the pinhole. [76]

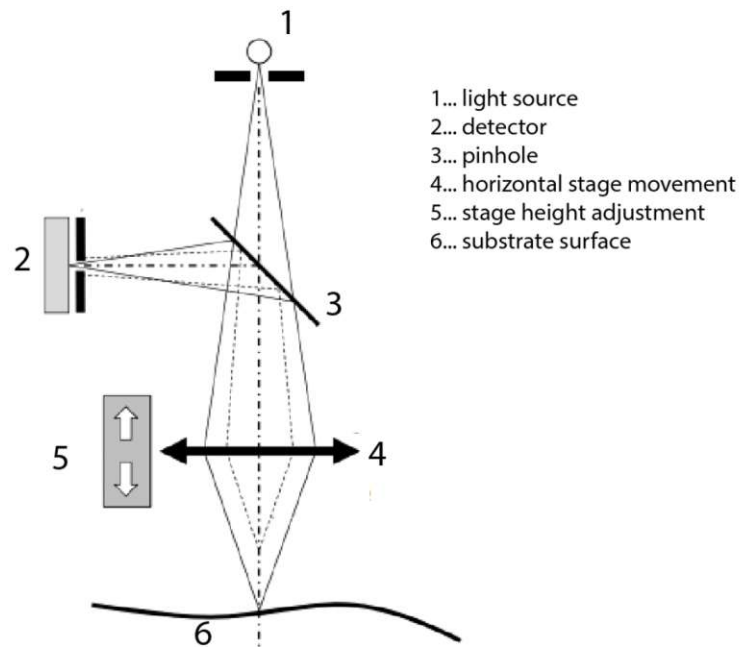


Fig. 4.9: Confocal configuration, adapted from [76].

## Deposition Technique

A series of Ti-Si-N and Ti-Si-B-N thin films were grown from mixed Ti/TiSi<sub>2</sub> and TiB<sub>2</sub> targets (from Plansee Composite Materials GmbH) using DC magnetron sputtering techniques in N<sub>2</sub>/Ar gas mixtures performed on an AJA International Orion 5 system. The mechanical and tribological properties have been optimized in a two-step alloying approach – the elemental composition and the deposition parameters have been gradually adjusted to meet the coatings' expectations.

Before placing the substrates in the deposition chamber, they have been ultrasonically cleaned with acetone and isopropanol for 5 min each. The PVD process can be mainly divided into three steps. First, the substrates were thermally cleaned for 20 min at 300 °C, followed by argon etching for 10 min at a bias voltage of -750 V to improve adhesion and remove any impurities from the surface. The etching process was conducted at a pressure of approximately 39 µbar by inserting 27.5 sccm Ar into the chamber. Before starting the actual deposition process, the targets were sputtered for 1 min with a closed shutter to clean the target surface from any impurities (oxygen) and to guarantee a stable sputter process. After opening the target shutters and turning on the bias voltage, the films were deposited by reactive DC magnetron sputtering in a gaseous mixture of argon and nitrogen. Based on the poisoning curves, the nitrogen (7.5 sccm) to argon (17.5 sccm) flow was 3:7, implying a constant deposition pressure of 4 µbar. During the entire process, the substrate temperature was set to 300 °C, and the substrate to target distance was positioned at 30 mm (literature review). To achieve a homogeneous coating, the substrates rotated during deposition.

In the first approach, Ti-Si-N and Ti-Si-B-N thin films have been deposited on silicon (20x7x0.38 mm<sup>3</sup>), austenite (20x7x0.8 mm<sup>3</sup>), and single-crystalline Al<sub>2</sub>O<sub>3</sub> (sapphire) (10x10x0.53 mm<sup>3</sup>) substrates, by reactively sputtering Ti/TiSi<sub>2</sub> targets with Si content of 10, 15, 20 and 25 at.% within the target (Si content given in x, Ti<sub>1-x</sub>Si<sub>x</sub>), for 60 min. For simplicity reasons the target notation is used as Ti/TiSi<sub>2</sub>, mentioning the overall Si content. As seen in Table 5.1, the applied bias voltage varied between -60 V, -80 V, and -100 V for depositions with a

target Si content of 15 at.%, and the applied current altered between 1.00 A, 1.25 A and 1.50 A for each Ti/TiSi<sub>2</sub> target. By adding the 2" TiB<sub>2</sub> target, the substrates have been co-sputtered with all 3" targets, varying the boron content by applying a current of 0.25 A, 0.5 A, and 0.75 A at the 2" cathode. This leads to overall 16 different chemical compositions within the Ti-Si-B-N system including also the ternary compositions.

**Table 5.1:** Preliminary composition

Targets	Si in Ti/TiSi <sub>2</sub> Target [at.%]	Bias voltage [V]	Ti/TiSi <sub>2</sub> current [A]	TiB <sub>2</sub> current [A]
3" Ti/TiSi <sub>2</sub>	15	-60	1.25	-
3" Ti/TiSi <sub>2</sub>	15	-100	1.25	-
3" Ti/TiSi <sub>2</sub>	15	-80	1.00-1.25-1.50	-
3" Ti/TiSi <sub>2</sub>	10	-80	1.00-1.25-1.50	-
3" Ti/TiSi <sub>2</sub>	20	-80	1.00-1.25-1.50	-
3" Ti/TiSi <sub>2</sub>	25	-80	1.00-1.25-1.50	-
2" TiB <sub>2</sub>	-	-80	1.25	0.25-0.5-0.75

After the first round of depositions, microhardness, as well as the structure and morphology of the thin films, have been analyzed to adapt the deposition parameters further. Based on the results obtained from SEM, the deposition rate was determined to adjust the deposition time for the second round to achieve a film thickness of approximately 2  $\mu\text{m}$ .

The findings from the first deposition set led to the choice of two promising Ti/TiSi<sub>2</sub>-containing targets with a Si content of 10 at.% and 15 at.%, respectively. Furthermore, the coating parameters have been optimized, as seen in Table 5.2. WC-Co inserts and WC-Co circular blanks have extended the substrates to determine the tribological behavior and improve the validity of the results for the individual application in the area of draw peeling.

**Table 5.2:** Selected target composition

Targets	Si in Ti/TiSi <sub>2</sub> Target [at.%]	Bias voltage [V]	Ti/TiSi <sub>2</sub> current [A]	TiB <sub>2</sub> current [A]
3“ Ti/TiSi <sub>2</sub>	10	-80	1.25	0.25-0.5-0.75
3“ Ti/TiSi <sub>2</sub>	15	-80	1.25	0.25-0.5-0.75
2“ TiB <sub>2</sub>	-	-80	1.25	0.25-0.5-0.75

The WC-Co circular blanks (parameters remained unchanged compared to the second round) have been re-coated after polishing the substrate surface to ameliorate the adhesion between the surface and coating. For the results and discussion part, the characterization methods described in Chapter 4 have been employed to determine structure and morphology, mechanical characteristics, and tribological properties and investigate the oxidation behavior.

## Experimental Data and Discussion

The following section applies the characterization methods explained in Chapter 4 to analyze the coatings deposited from the four different Ti/TiSi<sub>2</sub> targets co-sputtered with the TiB<sub>2</sub> target to enhance the mechanical and tribological properties of the thin films.

### 6.1 Preliminary study

Ti-Si-N coatings have been deposited from TiSi<sub>2</sub>-containing targets with different Si contents, ranging between 10 at.% and 25 at.%, to study the thin films' structural and mechanical evolution. In the first step, the Ti/TiSi<sub>2</sub> target containing 15 at.% Si was sputtered by applying different bias voltages (-60 V, -80 V, and -100 V) at the substrate. In the next step, each target was operated at a constant current of 1.00 A, 1.25 A, and 1.50 A, and finally, the TiB<sub>2</sub> target was added to receive the first insights of alloying boron to the ternary system.

#### 6.1.1 Structural Evolution and Morphology

To determine the coating thickness and gain information about the impact of Si on the morphology, cross-sections from the Ti-Si-N coatings deposited on silicon substrates have been recorded. Figure 6.1 illustrates the influence of the increasing Si content in the target on the deposition rate and morphology for a constant current of 1.00 A and 60 min deposition time. The white dashed line indicates the interface between the substrate and coating.



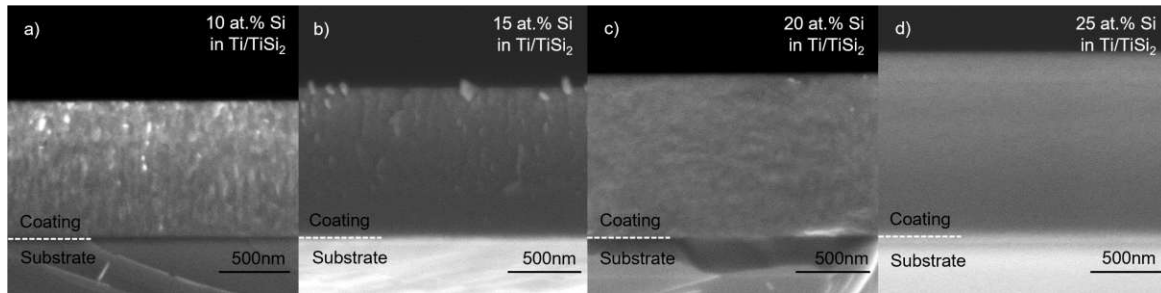


**Fig. 6.1:** SEM cross-sections from Ti-Si-N coatings sputtered from Ti/TiSi<sub>2</sub> targets with various Si content (a) 10 at.% (b) 15 at.% (c) 20 at.% and (d) 25 at.%

The selected cross-images measure a rising coating layer thickness between 926.7 nm and 1317 nm with growing silicon content in the target, indicating a higher deposition rate for targets with elevated Si concentration.

Comparing the SEM image resulting from the coating grown from the 10 at.% Si containing target (Figure 6.1a) up to 25 at.% one (Figure 6.1d), a strongly diverging morphology is recognizable. While the latter shows an amorphous-like structure, the thin film for 10 at.% Si containing target illustrates a finely-grained coating. Increasing to 15 at.% Si within the target, the amorphous Si<sub>3</sub>N<sub>4</sub> phase is strongly promoted in the surface near region. For even higher Si contents the nano-crystalline morphologies are predominant, leading most-likely to nanosized TiN crystals embedded in a Si rich matrix.

The SEM cross-sections confirm that with increasing Si content in the target, the amorphous Si<sub>3</sub>N<sub>4</sub> phase is more predominant, diminishing the TiN crystals - caused by the immiscibility of the two phases (see Chapter 2.2). This development towards a dense and homogeneous structure encourages the oxidation stability of the coating while preventing oxygen diffusion along grain boundaries during the formation of SiO<sub>2</sub> rich scales [9].

A similar morphological evolution for Ti-Si-N coatings with rising Si content in the target was also studied by Bartosik et al. [77].

The structural evolution of the Ti-Si-N films was analysed by X-ray diffraction. Using the Bragg Brentano configuration, the following X-ray diffraction patterns display the beam intensity as a function of the diffraction angle  $2\theta$ . The reference patterns are derived from the International Centre of Diffraction Data (ICDD) and are indicated by a dotted line. Overall, the resulting X-ray diffraction patterns follow the NaCl crystal structure type of TiN, illustrating the substrate material peaks of austenite (indicated by the smaller triangle symbol).

Figure 6.2 shows XRD analysis of Ti-Si-N deposited films sputtered with a Ti/TiSi<sub>2</sub> target of 15 at.% Si and a constant cathode current of 1.25 A varying the bias potential between -60 V, -80 V, and -100 V, respectively. While a bias voltage of -60 V depicts a preferred [111] orientation and a small peak at [220], the superior peak intensity for the [111] orientation is barely visible anymore at an applied bias of -80 V. Thus, with increasing bias voltage, the

preferred crystal growth orientation changed from [111] at -60 V to [200] orientation at -100 V.

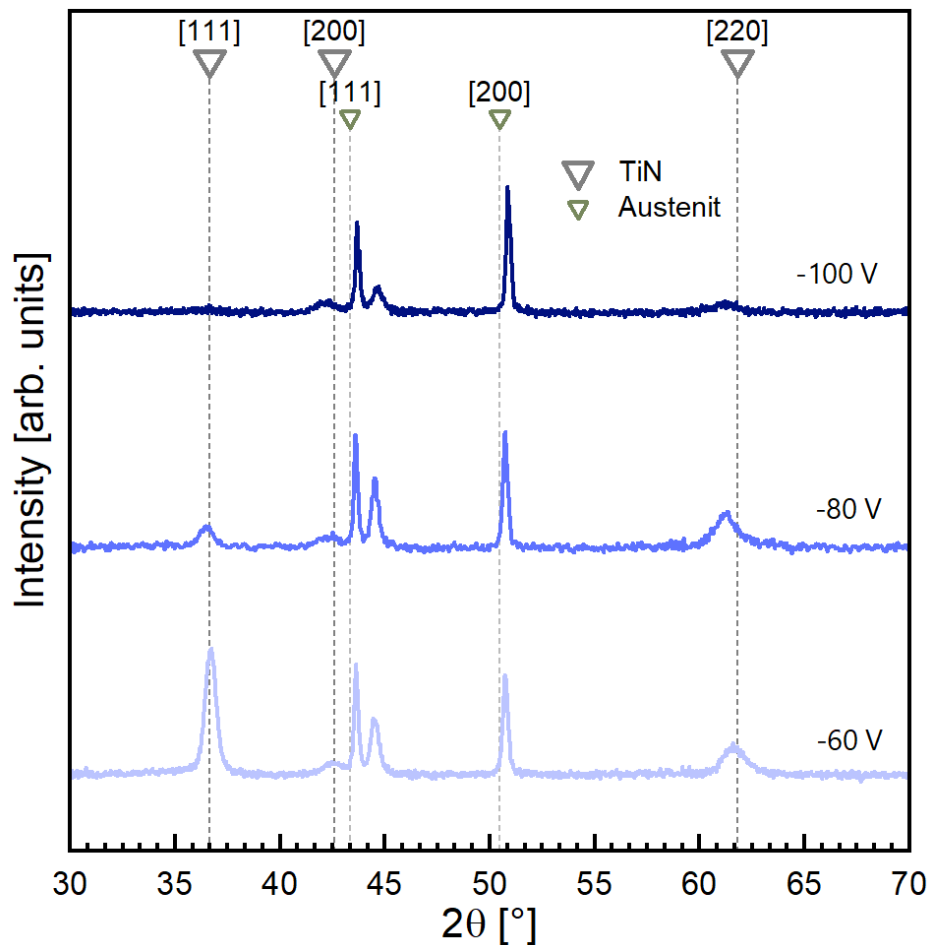


**Fig. 6.2:** X-ray Diffraction pattern for Ti-Si-N coatings with different bias potential using a Ti/TiSi<sub>2</sub> target with 15 at.% Si

This change in orientation relies on the principles of thermodynamics. Increasing the substrate bias leads to a higher ion bombardment, ultimately improving the film quality due to a denser structure. In extreme cases, bombarding Ar ions transfer energy and initiate re-sputtering or recrystallization. Therefore, the preferential orientation changes since the [200] orientation minimizes the surface free energy by allowing higher surface adatom mobility. Moreover, the surface energy is the decisive factor for small coating thicknesses, thus promoting the [200] orientation with the lowest surface energy. [78, 79]

Correlating the preferential orientation with the morphology investigated by the SEM cross-sections, the findings agree with Taghavi Pourian Azar et al. [80] claiming that Zone T of the structure zone model is determined by the [111] orientation based on the kinetic principles, showing thicker TiN grains as this is the case for the Ti-Si-N coatings deposited from the 15 at.% Si containing target and a bias voltage of -60 V (see Figure 6.3).

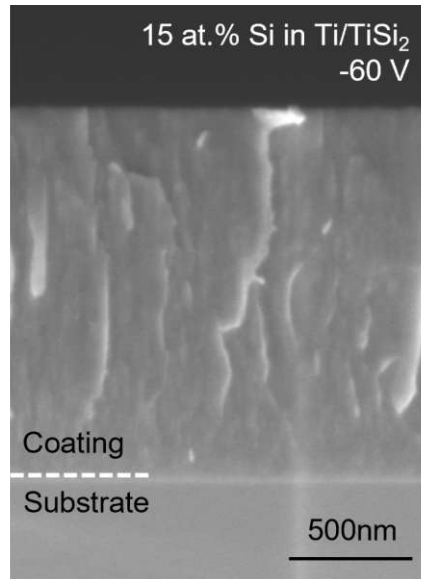


**Fig. 6.3:** SEM cross-section for Ti-Si-N coating sputtered from Ti/TiSi<sub>2</sub> target with 15 at.% Si and a substrate bias of -60 V

The contrary effect occurs in Figure 6.4 by increasing the cathode current from 1.00 A to 1.50 A, thus, shifting the preferred orientation from [200] to [111]. The Ti-Si-N coatings have been deposited by sputtering TiSi<sub>2</sub> targets with 15 at.% Si at a substrate bias of -80 V.

At a cathode current of 1.00 A, Figure 6.4 illustrates a preferred [200] orientation ascribed to lower surface energy. Though, with a rising target current (1.50 A), the [111] orientation is dominant, attributed to the fastest growing direction.

While the preferred orientation influenced by the substrate bias is directly related to the energy available for surface diffusion, the target current strongly affects kinetics of the sputter process. Applying high current results in a higher flux of sputtered atoms impinging the substrate surface, causing a rise also in the adatom mobility and encouraging the growth along [111] with the lowest strain energy [2]. This texture is also favored in the low temperature regime. [79]

Abadias [78] also suggests that the wear resistance is improved for TiN coatings growing along the [111] orientation (see chapter 6.2.4).

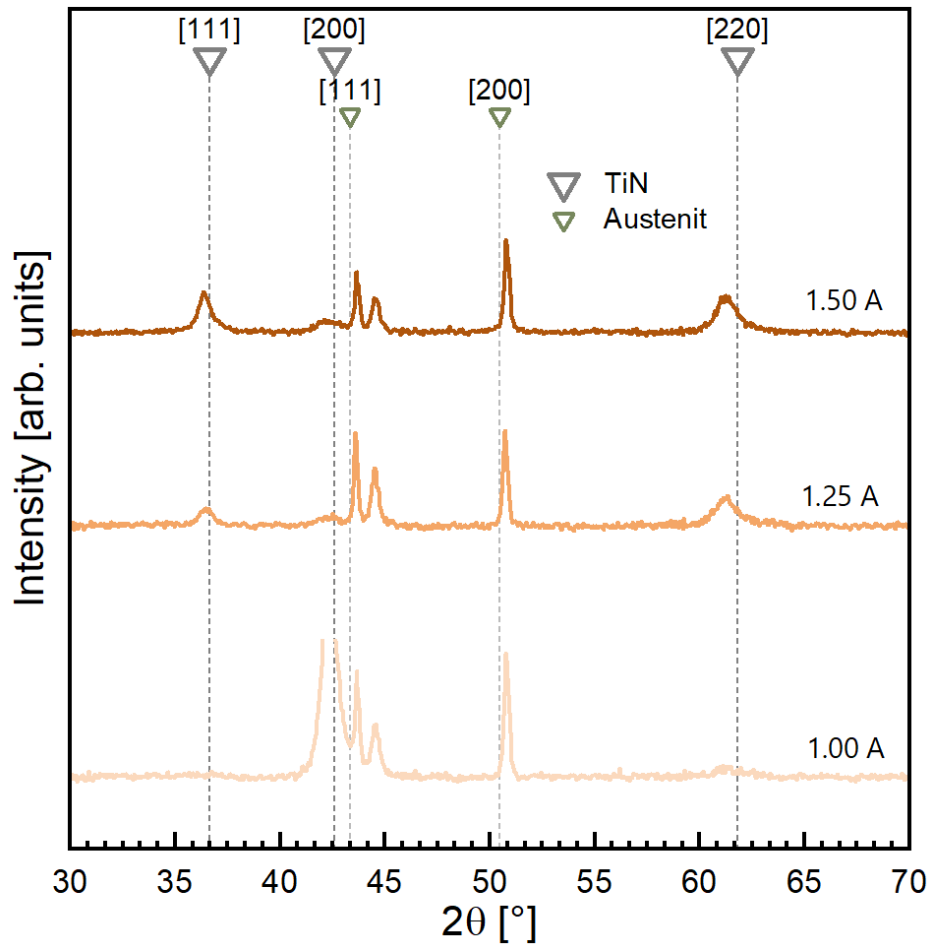
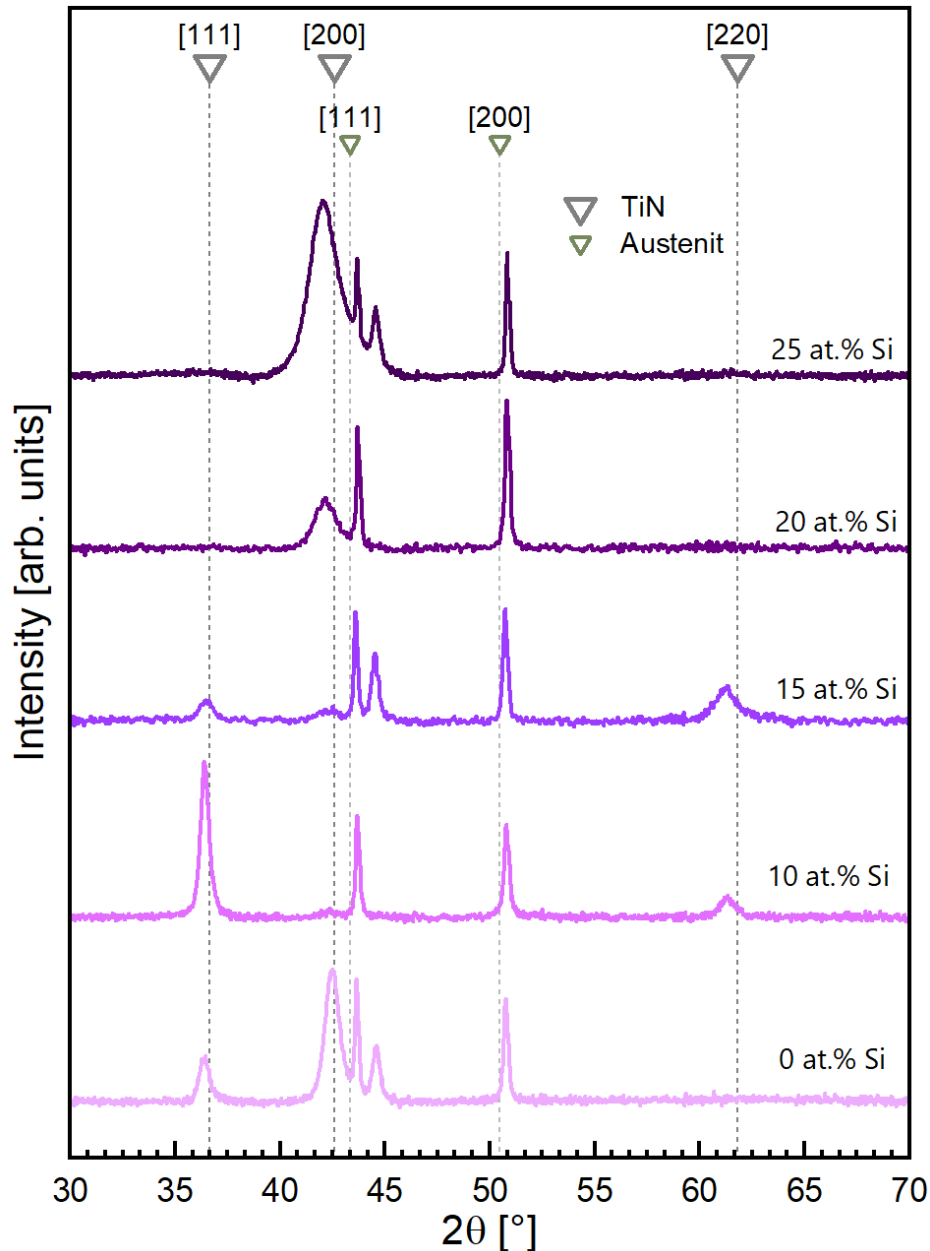


Fig. 6.4: X-ray Diffraction pattern for Ti-Si-N coating with increasing cathode current

Figure 6.5 shows the evolution of the preferred growth orientation with increasing Si content within the Ti/TiSi<sub>2</sub> target ranging from 0 to 25 at.% Si at a bias voltage of -80 V and a constant current of 1.25 A. Sputtering a Ti/TiSi<sub>2</sub> target with a Si content of 10 at.% exhibits a preferred [111] growth orientation. However, the peak intensity at 36.662°, attributed to the [111] orientation, significantly drops at a Si content of 15 at.% within the target. This trend continues and shows a noticeable change from the [111] to [200] orientation for a Si target content of 20 at.% and 25 at.% within the target material. Comparing the XRD pattern for 20 at.% with 25 at.%, a peak broadening and a slight shift to the left can be detected for the [200] orientation at 42.596°. The peak broadening phenomenon is also visible for the [111] orientation with 15 at.% Si in the target.



**Fig. 6.5:** X-ray Diffraction pattern of Ti-Si-N thin films with different Si content within the targets

These results follow several studies affirming that with increasing Si content, the preferred orientation changes from [111] to [200] and confirms both a peak broadening as well as a shift to the left [34, 38, 77, 81, 82]. The peak broadening mentioned above indicates a diminution of the TiN grain size, while the peak shift to the left implies increased residual compressive stresses in the crystal lattice due to a higher Si content within the thin film [11].

According to Arab Pour Yazdi et al. [81], the evolution of the preferred growth orientation can be attributed to the surface free energy. A smaller number of atoms within a nanocrystallite results in a gradual rise in surface free energy, hence, the preferential orientation changes

so that the nano-crystallites can reduce their free energy again [81]. Another explanation is provided by Cheng et al. [38], stating that due to the high internal stress in coatings with a low Si content, the [111] plane, characterized by the lowest strain energy, is the preferential orientation. However, with increasing Si content, the amorphous  $\text{Si}_3\text{N}_4$  layer at the TiN grain boundaries confines the mobility of the Ti atoms. Thus, the preferred growth orientation changes to the least dense plane (110) corresponding to the [220] orientation. [38]

Another noteworthy observation is that no  $\text{Si}_3\text{N}_4$  or TiSi peak was detected, indicating that the sputtered Si is either solute or in an amorphous phase. This follows literature findings [10, 39, 82] and the above SEM results, showing a nanocomposite structure. In the case of Hyun Kim et al. [82], the high Si content resulted in both an amorphous  $\text{Si}_3\text{N}_4$  and free Si in the coating due to limited nitrogen flow reacting with Si. Moreover, Cheng et al. [38] claim that the cohesive bond between the two phases results in a lower porosity at the grain boundaries and thus prevents the diffusion of Ti atoms. Overall, Abadías [78] notes that the alloying of transition metal nitrides encourages the [200] texture due to renucleation processes.

The diffraction patterns from Figure 6.6 show the co-sputtering of a 3" Ti/TiSi<sub>2</sub> target containing 15 at.% Si running at a constant current of 1.25 A and a 2" TiB<sub>2</sub> target operated at various constant currents between 0 A and 0.75 A to obtain coatings with increasing boron content.

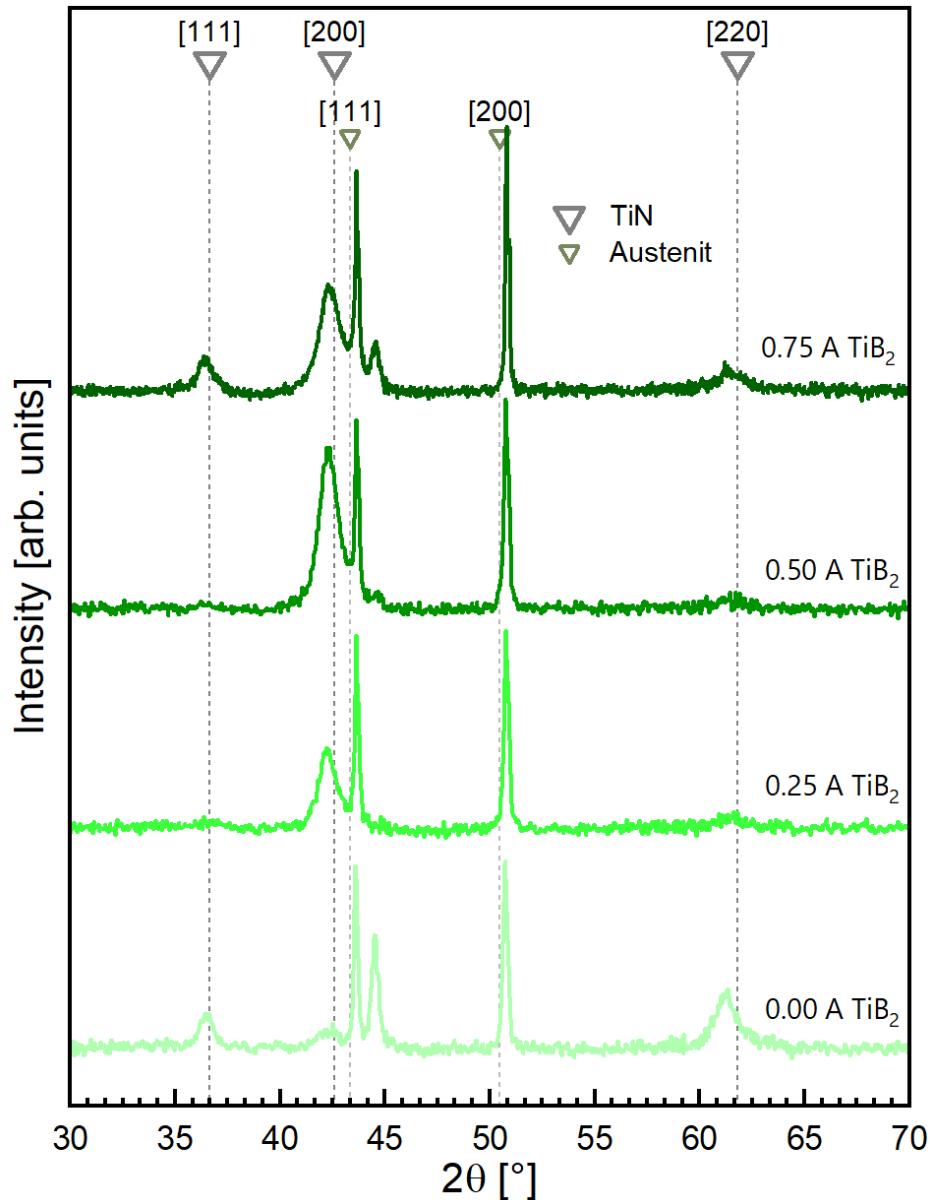


**Fig. 6.6:** X-ray Diffraction Pattern for Ti-S-B-N coatings with different  $2''$   $\text{TiB}_2$  cathode current

All coatings containing boron clearly exhibit a preferred [200] orientation. With an increasing  $2''$  target current, a peak broadening is evidenced. According to the literature, the broadening phenomena confirm a growing anisotropy of the nano-crystalline domains leading to coherently diffraction within the coating [4]. Subsequently, the XRD patterns verify the SEM results (Figure 6.14), illustrating that alloying boron to the ternary system results in a more random crystalline phase orientation and especially a decreased grain/crystallite size [3].

Compared to that, Fabrizi et al. [9] detected  $\text{TiB}_2$  peaks in the Ti-Si-B-N coatings; however, the thin films in this work exhibit a small amount of boron, thus only present in an amorphous phase.

## 6.1.2 Mechanical properties

Figure 6.7 illustrates the hardness of Ti-Si-N coatings as a function of the substrate bias in the range of -60 V to -100 V, for the coating grown from a Ti/TiSi<sub>2</sub> target with 15 at.% Si at a constant current of 1.25 A.

The hardness reaches a maximum of  $35.7 \pm 0.96$  GPa at a bias voltage of -80 V and drops again to  $31.1 \pm 0.96$  GPa at -100 V.

As already discussed in the XRD analysis, a rising bias voltage is linked to an intensified ion bombardment, thus affecting the surface diffusion during film growth. Studies affirm that the increasing hardness by ion bombardment, on the one hand, results from densification and a decrease in particle size. On the other hand, the initial rise can be attributed to residual stresses induced by the arriving adatoms. However, a further increase of the bias voltage leads to heightened adatom mobility fostering the growth of larger grains which is detrimental to the hardness. [83]

This effect was also visible in the changing growth orientation in the XRD patterns (see Figure 6.2).

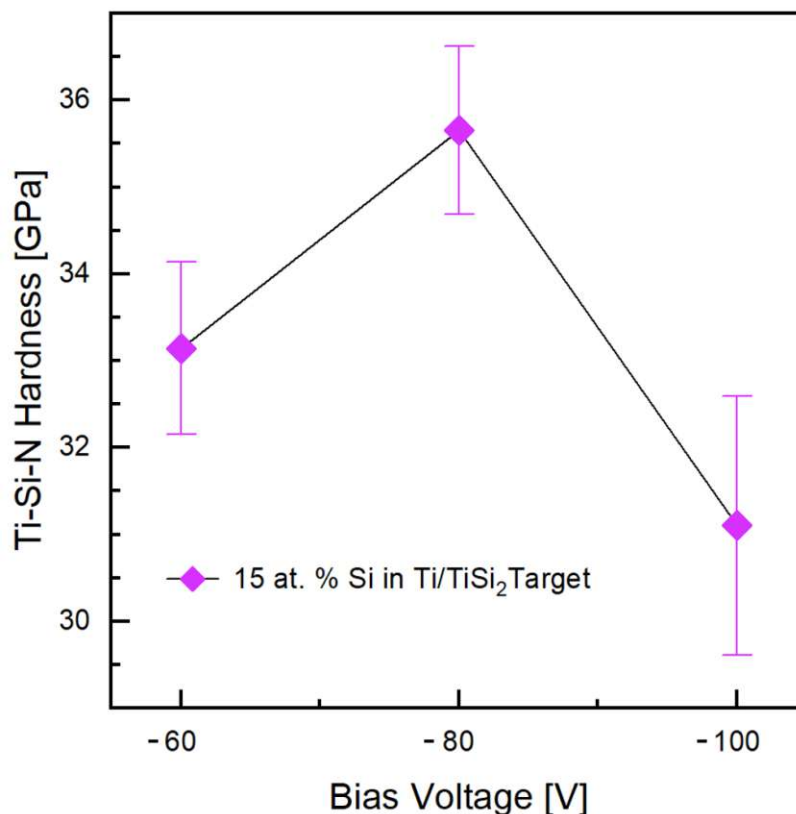


Fig. 6.7: Hardness of Ti-Si-N coatings at different substrate bias

Another crucial determinant for the hardness and Young's Modulus of Ti-Si-N coatings is the Si content in the target, as shown in Figure 6.8. The points connected by a line correspond



to a specific constant cathode current, as labeled in the figure.

Regardless of the target current, each line reaches a climax at a Si content of 15 at.% in the target ranging between 30 GPa and nearly 36 GPa, followed by a sharp decline for higher Si contents. The maximum hardness value of  $35.7 \pm 0.96$  GPa was measured at 1.25 A, while a constant current of 1.00 A barely reaches a hardness of 30 GPa for the same target. Nevertheless, this value is still slightly harder than the hardest coating deposited at 25 at.% Si within the Ti/TiSi<sub>2</sub> target, corresponding to  $29.1 \pm 1.18$  GPa, operated at a constant current of 1.25 A. These findings clearly confirm a significant hardness loss for thin films sputtered from a target with more than 15 at.% Si.

Regarding the applied constant current, 1.25 A results in the hardest coatings, except for 10 at.% Si within the target, which yields the highest hardness value of  $31.4 \pm 1.83$  GPa at a constant current of 1.50 A. In comparison, setting the target current to 1.00 A deposits the least hard coatings, regardless of the Si content.

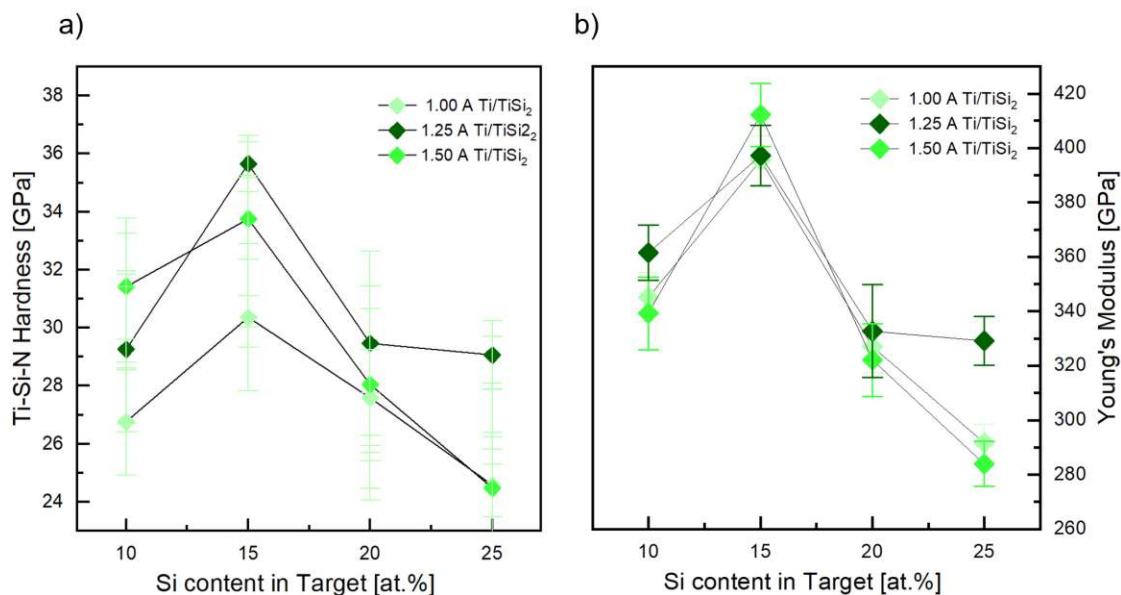


**Fig. 6.8:** Influence of the Si content in the target on the (a) hardness and (b) Young's Modulus of Ti-Si-N coatings sputtered at different cathode current

A similar dependence of the hardness on the silicon content is confirmed by several authors [6, 82, 84]. The initial hardness increase is correlated to the evolution of an amorphous Si<sub>3</sub>N<sub>4</sub> phase, coinciding with a diminution of TiN crystallites, as shown in the XRD results. The ternary Ti-Si-N system (see Chapter 2.2) provokes the formation of super-hard nanocomposite structures. The nc-TiN is embedded in an a-Si<sub>3</sub>N<sub>4</sub> matrix which prevents crack formation; thus, the high density of grain boundaries increases hardness [82].

Patscheider et al. [84] link the hardness evolution to the nanocomposite's morphological characteristics. Suggesting that the hardness falls when the mean distance between the

nanocrystallites is too large, which is correlated to a rising thickness of the amorphous phase [84].

Based on the different deposition parameters and techniques, studies affirm a maximum hardness at a silicon content of 4.4 at.% (41 GPa), 8 at.%, and 11at.% (38 GPa) Si in the films [81, 82, 85]. Comparing Figure 6.8a to Figure 6.8b, an almost linear relationship between the hardness and Young's modulus of the Ti-Si-(B-)N film can be assumed, which is following studies from [6]. After reaching a peak of  $412.2 \pm 11.68$  GPa for a silicon content of 15 at.% at 1.50 A, the curve shows a steep decline, virtually independent of the target current, indicating that increasing amorphous share ( $a\text{-Si}_3\text{N}_4$ ), the Young's modulus considerably decreases.

For the deposition of Ti-Si-B-N, the 2"  $\text{TiB}_2$  target varied between a cathode current of 0.25 A and 0.75 A, while the 3"  $\text{TiSi}_2$  target current is set to 1.25 A. Figure 6.9 illustrates the influence of the  $\text{TiB}_2$  current on the hardness and Young's modulus on the Ti-Si-B-N coatings by connecting the related data points with a line based on the respective  $\text{TiSi}_2$  target.

The slopes for both figures suggest a more or less linear decline in hardness and Young's modulus by increasing the  $\text{TiB}_2$  current, showing elevated mechanical properties for the  $\text{TiSi}_2$  target with 15 at.% Si, followed by 10 at.% Si, while 20 at.% and 25 at.% Si in the target is at the bottom end (in line with the results of the Ti-Si-N coatings).

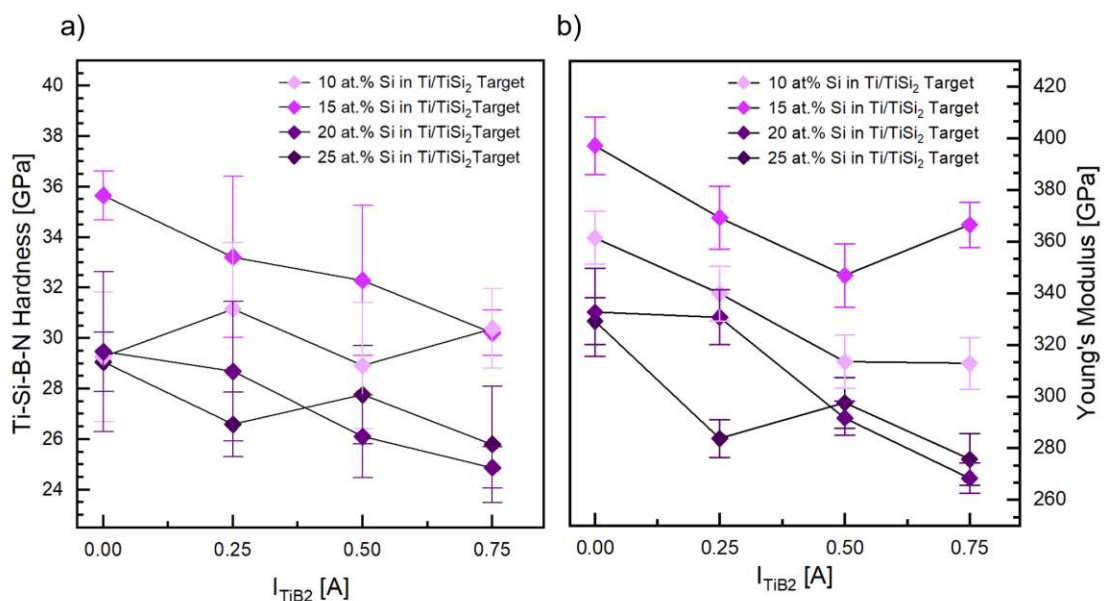


**Fig. 6.9:** Evolution of the (a) Hardness and (b) Young's Modulus for Ti-Si-B-N coatings as a function of the target current

As discussed in Chapter 2.4, alloying boron to the ternary Ti-Si-N system improves the tribological behavior of the thin films but at the expense of the coating's mechanical properties. The first data point on the left refers to the hardness and Young's modulus of Ti-Si-N coatings,

followed by a slight decline for Ti-Si-B-N coatings. For instance, the hardest Ti-Si-N coating with 15 at.% Si declines by 2 GPa down to  $33.2 \pm 3.19$  GPa, operating the  $\text{TiB}_2$  target at 0.25 A. Only the  $\text{TiSi}_2$  target with 10 at.% Si represents an exception by increasing its hardness value from  $29.3 \pm 2.58$  GPa to  $31.2 \pm 2.62$  GPa, operating the  $\text{TiB}_2$  target at 0.25 A and generally representing a more or less fluctuating hardness curve. A moderate hardness loss of maximum 5 GPa for each  $\text{TiSi}_2$  target composition is recorded with increasing  $\text{TiB}_2$  target current.

In the case of Young's modulus, alloying boron to the coating system underlines that an increase in amorphous share leads to a decrease in stiffness of the coating, again illustrating a linear behavior between a) hardness and b) Young's modulus for Ti-Si-B-N coatings.

### 6.1.3 Deposition rate

Figure 6.10 reveals a linear correlation between a rising cathode current and an increased deposition rate. These findings explain the increase in coating thickness for films deposited at a higher target current. Considering the influence of the 2<sup>nd</sup> target current on the deposition rate, the deposition time was adapted to achieve a coating thickness of about 2  $\mu\text{m}$  which might also influence the achieved coating hardness (see chapter 6.2.3).

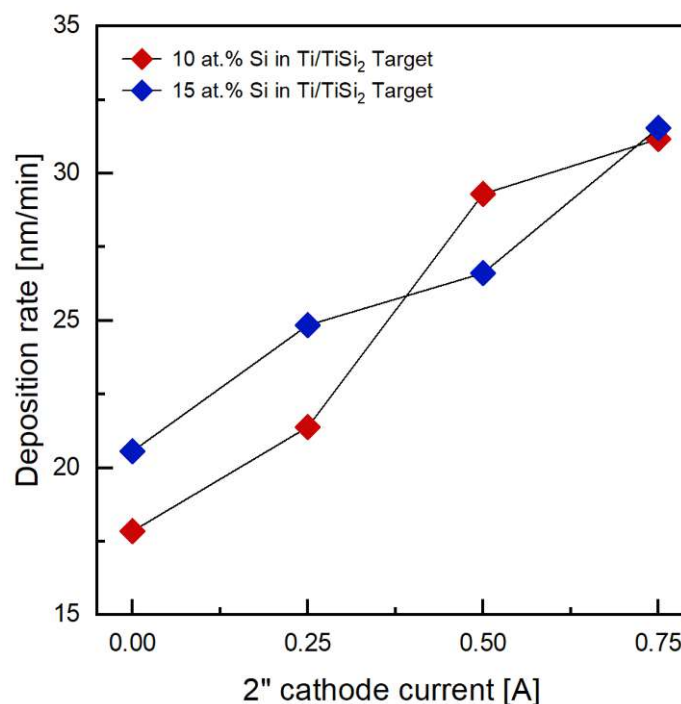


Fig. 6.10: Deposition rate as a function of the  $\text{TiB}_2$  target current

## 6.2 Optimized parameter variations

The results from the preliminary study helped to refine the deposition parameters, such as the substrate bias (-80 V) and 3" cathode current (1.25 A), and opt for the most promising Ti/TiSi<sub>2</sub> targets (10 at.% and 15 at.% Si).

For the selected coating parameters, new substrate materials have been added (WC-Co) and further experiments with regards to oxidation and tribology have been conducted, with the aim of determining the optimum alloying of boron to Ti-Si-N thin films.

### 6.2.1 Elemental composition

The X-ray fluorescence results illustrated in Figure 6.11 confirm that with a rising TiB<sub>2</sub> target current, the boron content in the thin films increases. This correlation is confirmed by Asempah et al. [43], increasing the boron content by raising the power at the target from 0 W to 120 W.

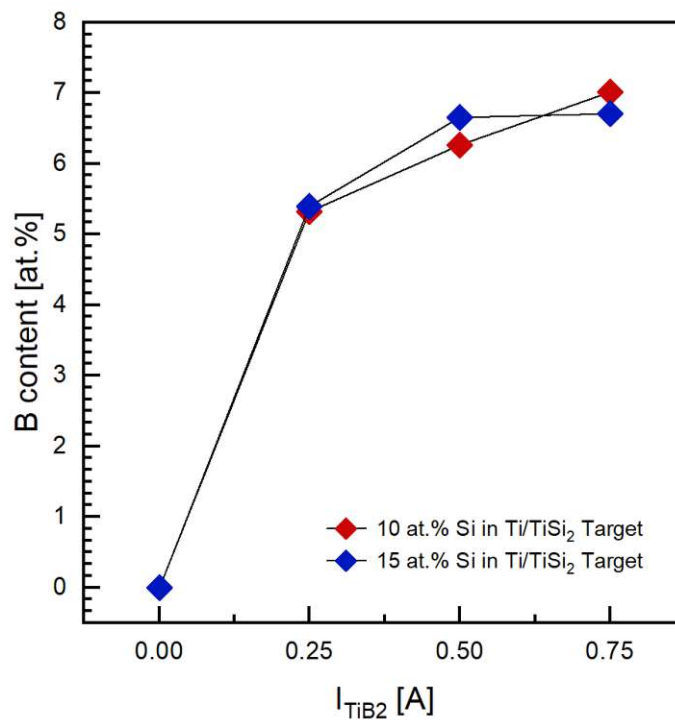


**Fig. 6.11:** Boron content in the coating as a function of the target current

Changing the boron content in the coatings consequently alters the elemental composition. Figure 6.12 depicts the share of silicon as a function of boron in the thin films. An almost consistent depression is drawn for the share of Si with rising boron content. This phenomenon is due to the reaction of N with B, as can be seen in Figure 6.13, thus reducing the binding reaction between Si and N to form Si<sub>3</sub>N<sub>4</sub>. The only exception is the Ti-Si-B-N coating

deposited at 15 at.% Si in the target and a  $\text{TiB}_2$  target current of 0.5 A, showing a slight increase in Si content.

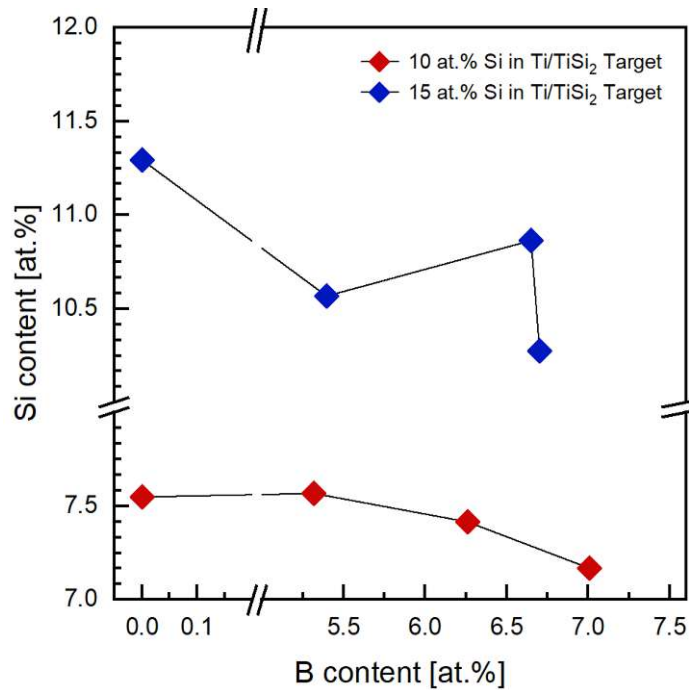


**Fig. 6.12:** Share of Si in the coating as a function of B

The elemental composition for the two different coating series is presented in a ternary phase diagram for the respective Si content, see Figure 6.13.

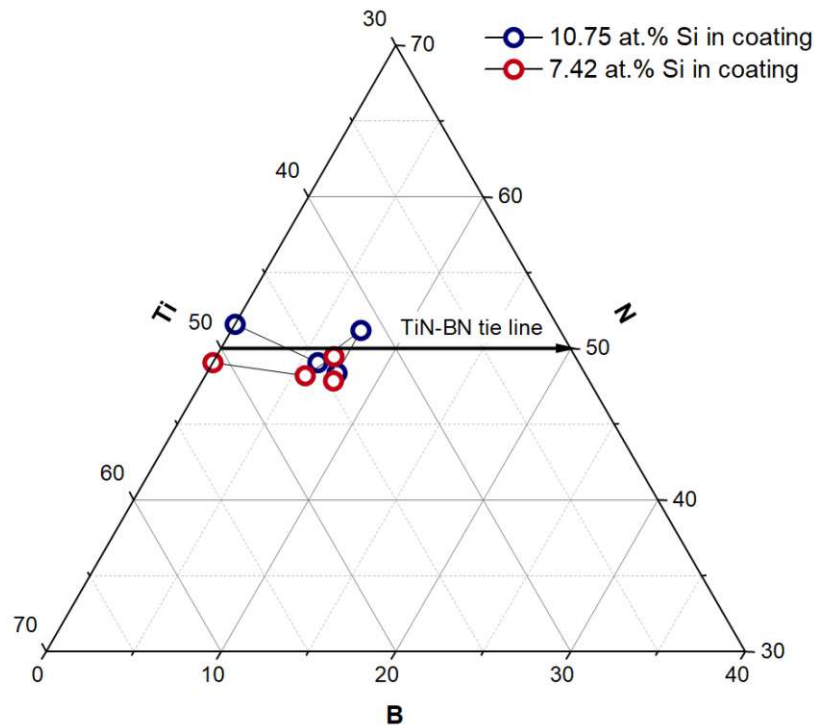


**Fig. 6.13:** Ternary phase diagram for 10.75 at.% Si (blue) and 7.42 at.% Si (red) in the coating

Increasing the boron content within the coatings can generally lead to forming a BN or  $\text{TiB}_2$  phase. In both cases, a clear tendency towards forming an a-BN phase with increasing boron content is evident. These findings are in accordance with literature stating that a B content below about 8 at.% favors the formation of a BN phase, while the  $\text{TiB}_2$  phase is encouraged at a higher B content (see chapter 2.3) [7]. Furthermore, Hahn et al. [86] investigated a difference between reactively and non-reactively co-sputtered Ti and  $\text{TiB}_2$  targets. While the latter reacts along the TiN- $\text{TiB}_2$  tie line, reactive sputtering promotes bindings along the TiN-BN tie line [86].

Table 6.1 summarizes the elemental coating compositions based on XRF results.

**Table 6.1:** Elemental composition obtained from XRF results

Si in Ti/TiSi <sub>2</sub> Target	TiB <sub>2</sub> I	Ti	Si	B	N
[at.%]	[A]	[at.%]	[at.%]	[at.%]	[at.%]
10	0.00	47.08	7.55	0.00	45.37
10	0.25	42.78	7.57	5.32	44.76
10	0.50	40.75	7.41	6.26	46.01
10	0.75	41.61	7.17	7.01	44.63
15	0.00	42.93	11.29	0.00	45.78
15	0.25	40.40	10.57	5.39	44.11
15	0.50	37.10	10.86	6.65	45.89
15	0.75	39.84	10.27	6.70	43.64

## 6.2.2 Structure and morphology

The SEM cross sections recorded in Figure 6.14 illustrate the morphology of the Ti-Si-B-N coatings deposited at a constant 3” cathode current of 1.25 A and a growing current for the TiB<sub>2</sub> target to elevate the boron concentration in the coatings.

All three cross-sections represent a dense and relatively featureless SEM image, though the cross-section with the highest applied target current seems remarkably smooth and homogenous (Figure 6.14c). In comparison, Figure 6.14a shows a growth progression, starting from an amorphous-like structure at the interface to a more structured and finely-grained surface at the top. This evolution can result from the growth development over the coating thickness, as described by Andersen (see Chapter 3.2).

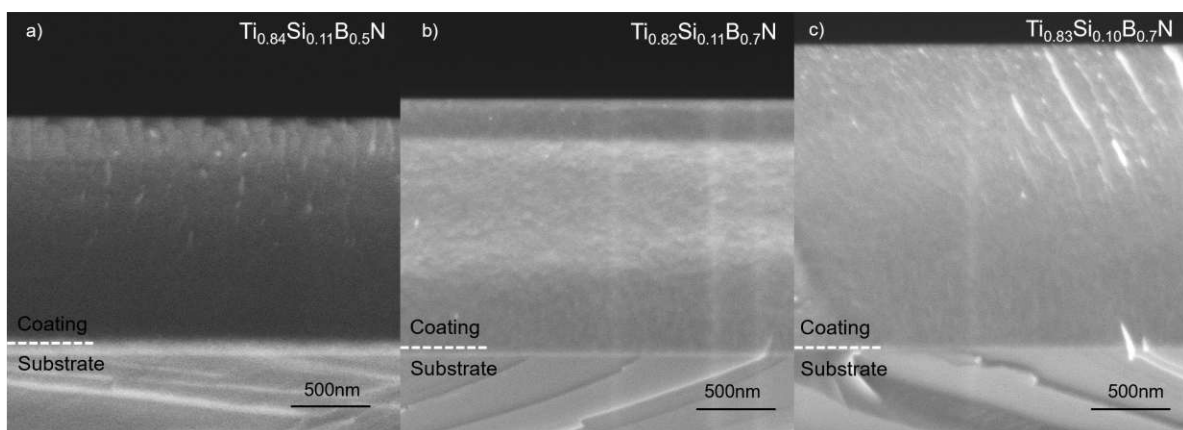


**Fig. 6.14:** SEM cross-sections for Ti-Si-B-N coatings co-sputtered from Ti/TiSi<sub>2</sub> with 15 at.% Si and a rising cathode current of (a) 0.25A (b) 0.50A and (c) 0.75A for the TiB<sub>2</sub> target

The X-ray diffraction patterns in Figure 6.15 aggregate the results for both selected Ti/TiSi<sub>2</sub> targets, illustrating the 10 at.% Si target in red and 15 at.% Si in blue, with increasing color brightness referring to a higher boron content in the thin film. This color scheme is applied to all the following graphs. The XRD patterns on the left side are the coatings deposited on austenite. The blue graphs confirm the results from the preliminary coatings, shown in Figure 6.6. Compared to that, the Ti/TiSi<sub>2</sub> target with 10 at.% Si presents a very pronounced [111] orientation with increasing TiB<sub>2</sub> target current. The increased peak intensity in comparison to the 15 at.% Si can be traced back to the elemental composition shown in Table 3 and Figure 6.12. An increasing B content corresponds to a slight decrease in Si content. As mentioned for Figure 6.5, a lower Si content is characterized by [111] orientation, changing to [200] for higher shares of Si.

Additionally, the peaks are broader for a higher Si content in the coatings due to a higher Si<sub>3</sub>N<sub>4</sub> share leading to smaller TiN grains.

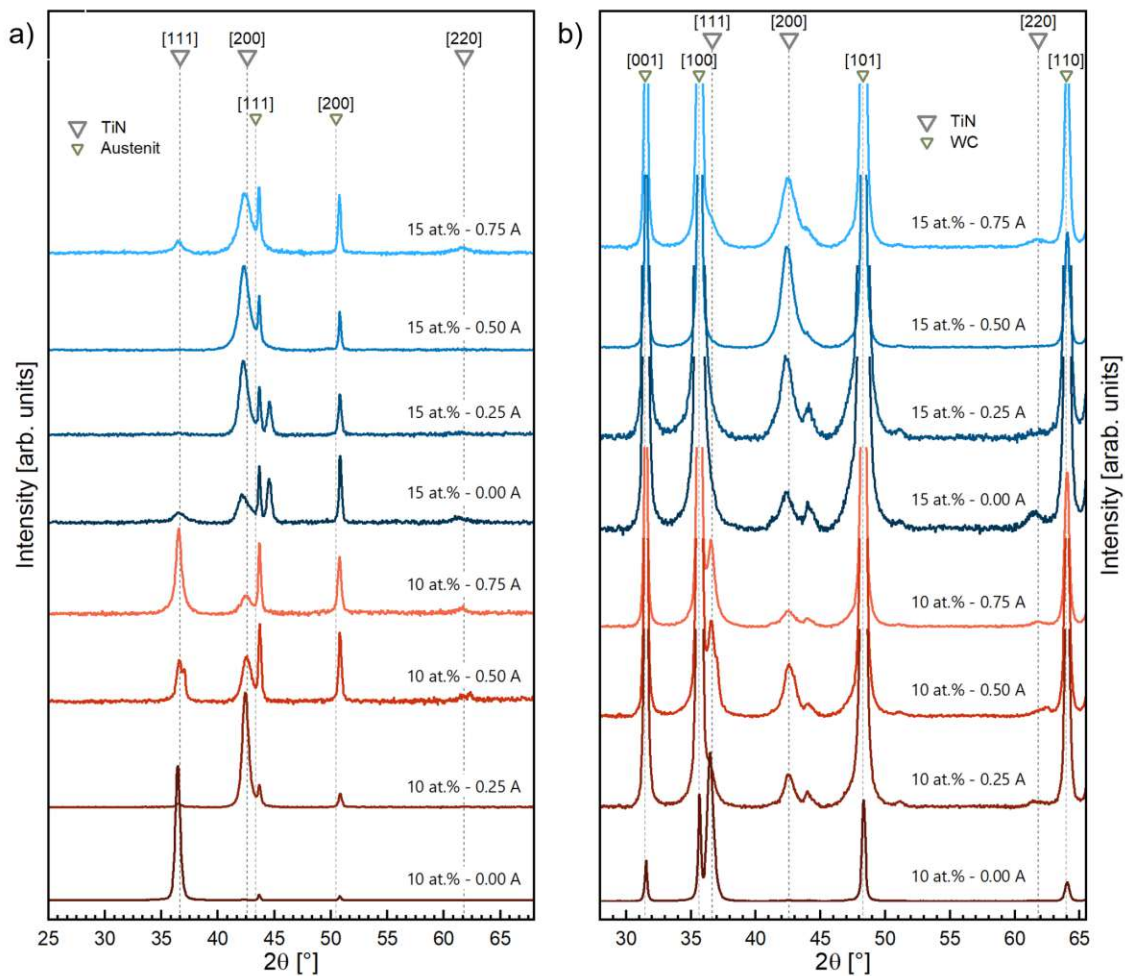


**Fig. 6.15:** X-ray patterns for Ti-Si(-B)-N coatings on (a) austenite and (b) WC-Co sorted by Ti/TiSi<sub>2</sub> target with increasing 2'' TiB<sub>2</sub> target current



Figure 6.15b detects the XRD signals from Ti-Si-B-N coatings deposited on WC-Co. Overall, the results show the same trend as on the left side, however the signals from the WC-Co substrate display extreme intensities, as indicated by the dotted line for the WC reference pattern.

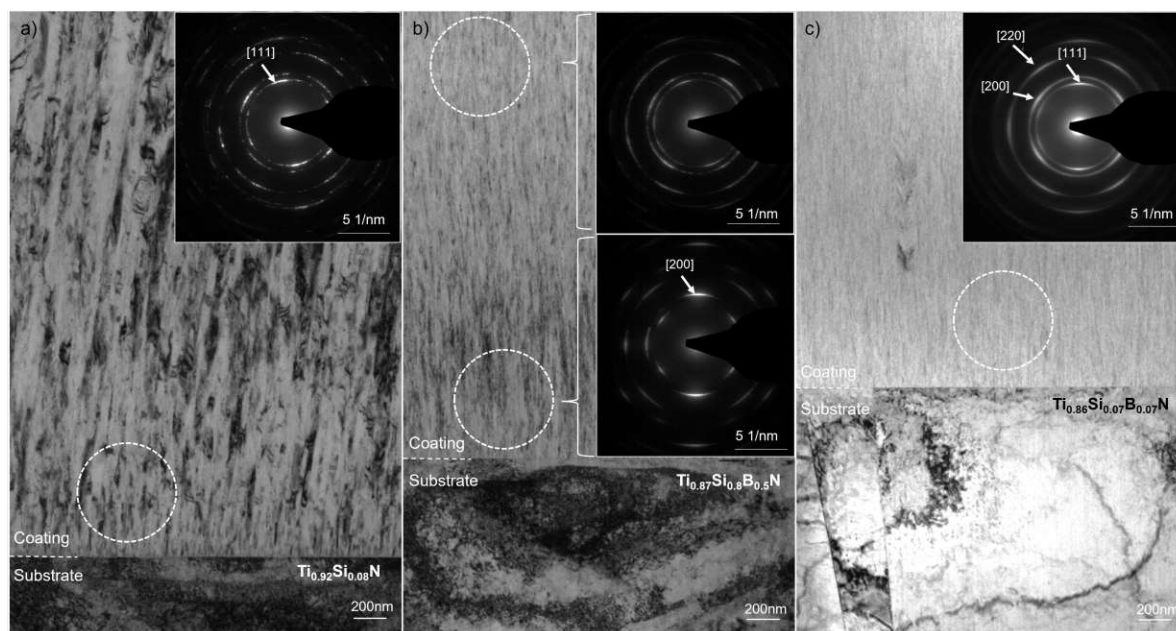


**Fig. 6.16:** TEM bright field images and selected area electron diffraction (SAED) pattern for (a)  $\text{Ti}_{0.92}\text{Si}_{0.08}\text{N}$ , (b)  $\text{Ti}_{0.86}\text{Si}_{0.07}\text{B}_{0.07}\text{N}$  and (c)  $\text{Ti}_{0.87}\text{Si}_{0.07}\text{B}_{0.06}\text{N}$  coatings with increasing boron content, sputtered from Ti/TiSi<sub>2</sub> containing 10 at.% Si

Figure 6.16 shows bright field (BF) images of the film structure with the corresponding selected area diffraction (SAED) pattern of the  $\text{Ti}_{0.92}\text{Si}_{0.08}\text{N}$ ,  $\text{Ti}_{0.87}\text{Si}_{0.07}\text{B}_{0.06}\text{N}$  and  $\text{Ti}_{0.86}\text{Si}_{0.07}\text{B}_{0.07}\text{N}$  coatings sputtered from the Ti/TiSi<sub>2</sub> target containing 10 at.% Si and co-sputtered TiB<sub>2</sub>, recorded by TEM. From left to right the boron content increases from 0 at.% (a) to 5.32 at.% (b) and 7.01 at.% (c), significantly changing the structural evolution from columnar grains to a very finely-grained/nano-crystalline morphology. The TEM analysis for  $\text{Ti}_{0.92}\text{Si}_{0.08}\text{N}$  (Figure 6.16a) presents a randomly oriented crystal structure characterized by a high dislocation density, with preferred [111] growth orientation of the TiN grains, in accordance to the findings by Hyun et al. [82]. Alloying 5.32 at.% boron to the system results in a considerably more finely grained structure, with higher grain density close to the substrate interface and fewer as well as smaller grains with increasing film thickness. In the substrate-near region, the SAED pattern implies a cubic crystal structure with a preferred [200] orientation, while a decreased diffraction intensity is evident close to the coating surface, describing isotropic behaviour.

The  $\text{Ti}_{0.86}\text{Si}_{0.07}\text{B}_{0.07}\text{N}$  (Figure 6.16b) coating with the highest boron content, exhibits a largely homogeneous, extremely fine-fibrous morphology, with preferential [111] and [200] orientation,

confirming the existence of TiN nano-crystallites. Similar findings are affirmed by Hahn et al. [86] for reactively sputtered Ti-Si-B-N coatings with 9 at.% B.

The obtained results are consistent with XRD results, confirming the existence of fcc-TiN nano-crystallites, for both Ti-Si-N and Ti-Si-B-N coatings and exhibiting a significant grain refinement with increasing boron content.

### 6.2.3 Mechanical properties

Figure 6.17 shows the a) hardness and b) Young's modulus of Ti-Si-(B)-N coatings as a function of the boron content. The coatings have been sputtered from a Ti/TiSi<sub>2</sub> target with 10 at.% (red) and 15 at.% (blue) Si at a constant current of 1.25 A and a varying cathode current for the TiB<sub>2</sub> target resulting in different B contents.

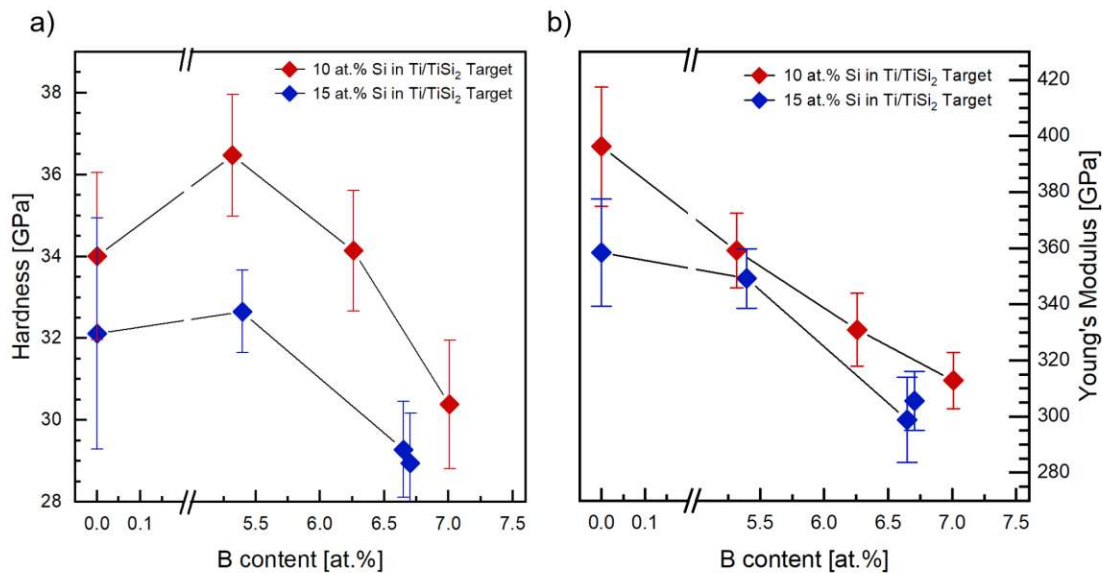


**Fig. 6.17:** Evolution of (a) hardness and (b) Young's modulus for Ti-Si-N coatings with increasing B content for selected Ti/TiSi<sub>2</sub> targets

Overall, the results agree with the findings from the first coatings. However, two particularities can be identified, deviating from the preliminary results. Firstly, the coatings deposited from the Ti/TiSi<sub>2</sub> target with 10 at.% Si achieves harder and more stiff coatings than the thin films from the 15 at.% Si target. Secondly, the hardness increases when boron is added in small amounts before it starts to decline. The superior mechanical properties for the 10 at.% Si set presumably results from the adjusted deposition time to produce thicker coatings, exhibiting, on average, a 5 GPa improvement. For example, the thin film sputtered at 0.25 A TiB<sub>2</sub> (5.32 at.% B) shows a rise in hardness from 31.16±2.62 GPa for the first coatings to a

maximum hardness of  $36.5 \pm 1.49$  GPa, characterized by a film thickness of 1283 nm and 1995 nm respectively.

On another note, the initial increase in hardness could be related to a strictly stoichiometric composition of the TiN phase at a small amount of boron (5.32 at.%) [5, 10].

However, with increasing boron content, the hardness of the thin film is dominated by the softer amorphous phase [43].

Attaining a high hardness while maintaining a low elastic modulus is desirable to resist plastic deformation [87]. Therefore, the ratio  $H^3/E^2$  is introduced and plotted against the boron content in Figure 6.18.

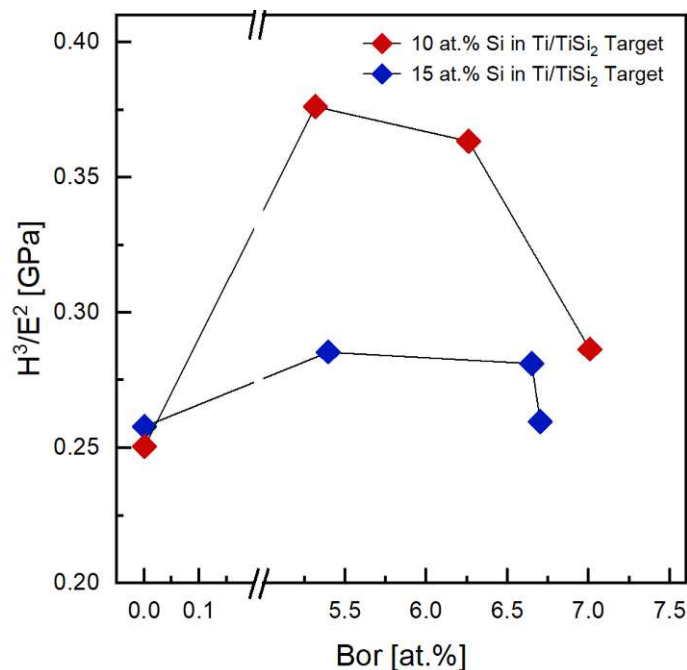


**Fig. 6.18:**  $H^3/E^2$  as a function over the boron content

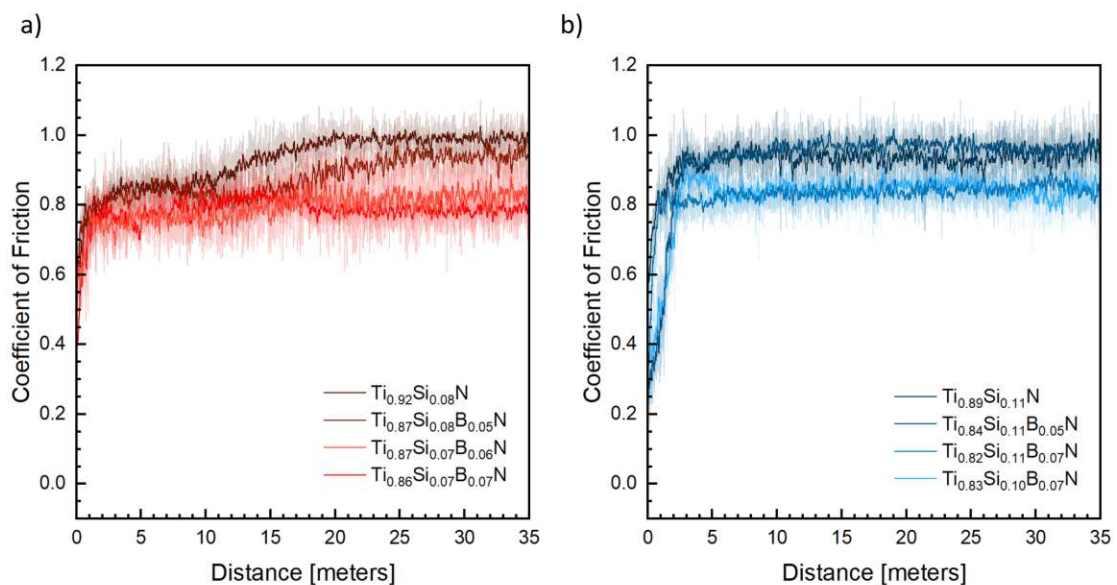
Adding the  $TiB_2$  target to the ternary coating system improves the resistance against plastic deformation, reaching a climax of 0.38 GPa and 0.29 GPa, for coatings co-sputtered with Ti/TiSi<sub>2</sub> containing 10 at.% Si and 15 at.% Si and a boron content of 5.32 at.% and 5.39 at.%, respectively, followed by a plateau and decline afterward due to a higher share of an amorphous phase. Furthermore, the ratio  $H^3/E^2$  provides information about the wear resistance of the coating [43].

Figure 6.17 and Figure 6.18 imply that small amounts of boron improve the micromechanical properties of Ti-Si-B-N coatings sputtered from Ti/TiSi<sub>2</sub> targets with 10 at.% and  $TiB_2$  targets, operated at a constant current of 1.25 A and 0.25 A, correspondingly.

## 6.2.4 Tribological behavior

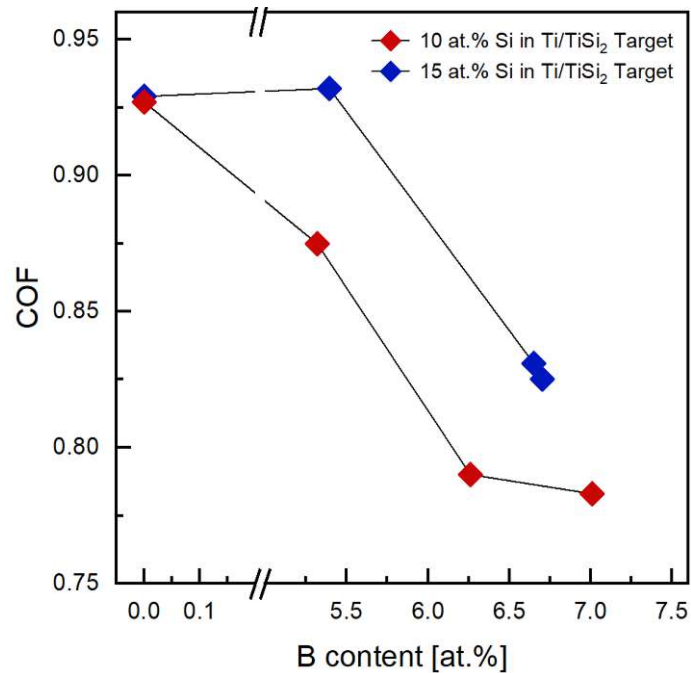
As described in Chapter 2.4, alloying boron to the ternary Ti-Si-N system enhances the tribological properties of the thin films. However, the high surface roughness of the WC-Co circular blanks resulted in poor coating adhesion, showing Zone I microstructure as defined by Thornton (see chapter 3.2) for the thin films. Subsequently, the substrates have been polished to improve coating-to-substrate adhesion and achieve improved and more stable tribological results.

Figure 6.19 illustrates the evolution of the coefficient of friction as a function of the sliding distance for the corresponding Ti/TiSi<sub>2</sub> targets by using a steel ball (100Cr6) as a counterpart.



**Fig. 6.19:** Evolution of the coefficient of friction as a function of the sliding distance for (a) 10 at.% Si and (b) 15 at.% Si in the Ti/TiSi<sub>2</sub> target

Smoothing the curves demonstrates that for the 10 at.% Si target (Figure 6.19a), the COF fluctuates on average between 0.78 and 0.93, compared to 0.83 and 0.93 for 15 at.% Si (Figure 6.19b). Both figures prove that a higher boron content in the coating (brighter colors) leads to a slightly decreased COF. Nevertheless, tribological behavior heavily depends on several complex parameters and the application environment [4].



**Fig. 6.20:** COF as a function of the boron content

The tribometer data is compromised in Figure 6.20, showing the COF for the two selected Ti/TiSi<sub>2</sub> targets as a function of the boron content in the coatings. A significant drop in the COF occurs between approximately 5.3 at.% and 6.6 at.% B, reducing the coefficient of friction by 0.1 from 0.93 to 0.83 in the case of 15 at.% Si in the target. For the Ti-Si-B-N coatings sputtered from Ti/TiSi<sub>2</sub> containing 10 at.% Si, the starting base is already lower at 0.88 and falls to 0.79 for a higher boron content. Further addition of boron shows a considerably flatter gradient, indicating that increasing the boron content further is less decisive than the initial B increase.

The experimental results are in accordance with literature showing a similar COF of 0.81 at room temperature [88].

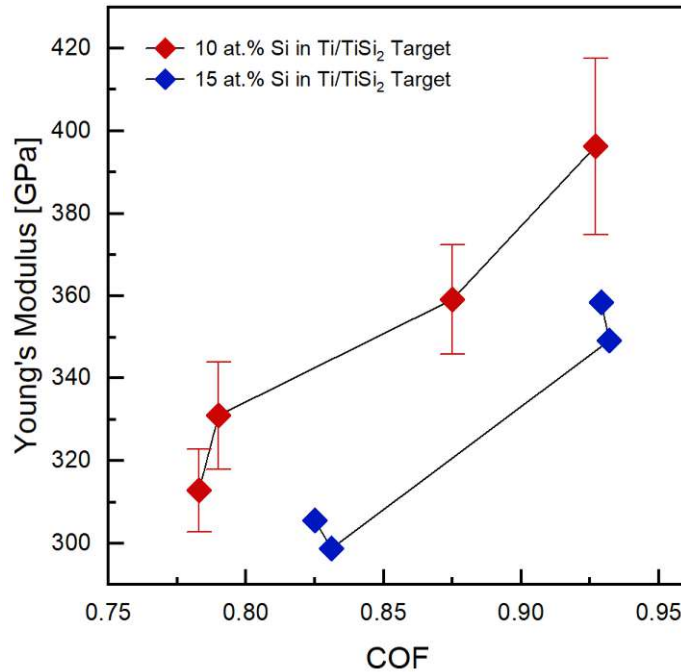


**Fig. 6.21:** Young's modulus as a function of the COF for the two selected Ti/TiSi<sub>2</sub> targets

Plotting the Young's modulus over the COF for the deposited Ti-Si-(B)-N coatings results in Figure 6.21. Both curves show a strong correlation, indicating that the COF decreases for coatings with a lower elastic modulus. Remembering the previous results that a rising boron content is associated with a declining Young's modulus and forming an  $\alpha$ -BN phase, Figure 6.21 suggests that the soft  $\alpha$ -BN phase promotes a decreasing COF. This assumption is confirmed by Asempah (2019) analyzing Ti-B-N coatings. According to literature, this can be ascribed to, on the one hand, a self-lubricating effect caused by the  $sp^2$  bonded-like structure, which is also characterized by a higher ductility, and on the other hand, the formation of a thin lubricating layer of the soft  $\alpha$ -BN phase [43, 89].

Contrary to the assumption and the results presented for the COF, the evolution of the wear rate shows the opposite trend. The coatings deposited from the Ti/TiSi<sub>2</sub> target containing 10 at.% Si recorded a brisk rise in the wear rate with increasing boron content in the thin films (Figure 6.22).

A possible reason for this might be related to the crystal growth orientation. As mentioned in the XRD analysis, coatings exhibiting a preferred [111] orientation for TiN indicate improved wear resistance [78]. Referring to Figure 6.15, the peak intensity at [111] for the Ti-Si-N coating is highly pronounced, while the Ti-Si-B-N coating with 0.25 Å for the TiB<sub>2</sub> target shows a preferred [200] orientation. Although Figure 6.22 reveals a clear trend for the evolution of the wear rate, it is worth mentioning that the variation ranges barely between  $1 \cdot 10^{-5}$  and  $8 \cdot 10^{-6}$  mm<sup>3</sup>/Nm.

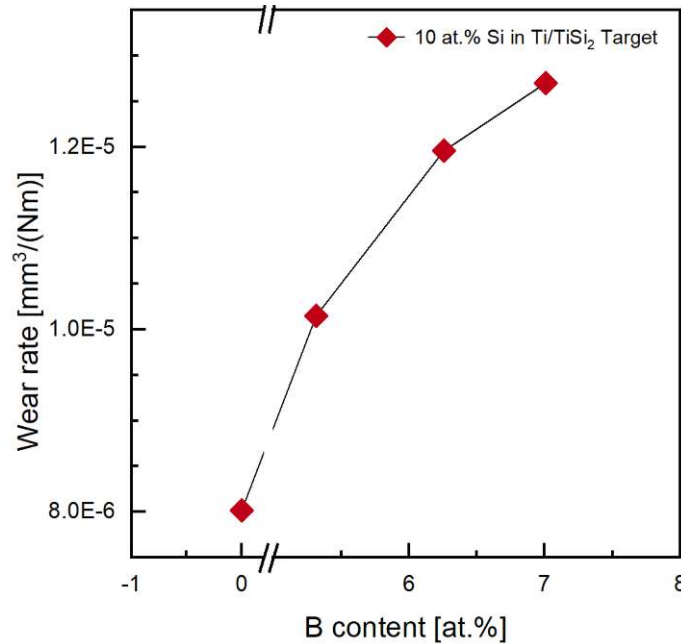


**Fig. 6.22:** Evolution of the wear rate as a function of the boron content for the Ti/TiSi<sub>2</sub> target with 10 at.% Si

### 6.2.5 Oxidation resistance

To investigate the coatings' oxidation behavior, the oxide layer thickness was determined by FIB and plotted as a function over the annealing time. Figure 6.23 shows the evolution of the oxide layer thickness after 10, 25, and 100 min, resulting in a parabolic behavior for both Ti/TiSi<sub>2</sub> targets.

Coatings grown from the Ti/TiSi<sub>2</sub> targets with 10 at.% Si (on average 7.42 at.% Si in the coatings) illustrate a steeper gradient than the films deposited by 15 at.% Si (on average 10.75 at.% Si in the thin films), proving that a higher share of Si positively impacts the oxidation resistance of thin films. While the curves in Figure 6.23a, which belong to the nc-TiN/a-BN coatings, follow the same trend, eventually reaching an oxide layer thickness between 433.7 nm and 507.8 nm (Ti<sub>0.86</sub>Si<sub>0.07</sub>B<sub>0.07</sub>N and Ti<sub>0.87</sub>Si<sub>0.08</sub>B<sub>0.05</sub>N, respectively), the evolution of the nc-TiN/a-Si<sub>3</sub>N<sub>4</sub> coating (Ti<sub>0.92</sub>Si<sub>0.08</sub>N) shows a significantly flatter gradient, developing a minimum thickness of 319.5 nm after 100 min, which is comparable to the behavior of the Ti-Si-B-N coatings containing on average 10.75 at.% Si (see Figure 6.23b).

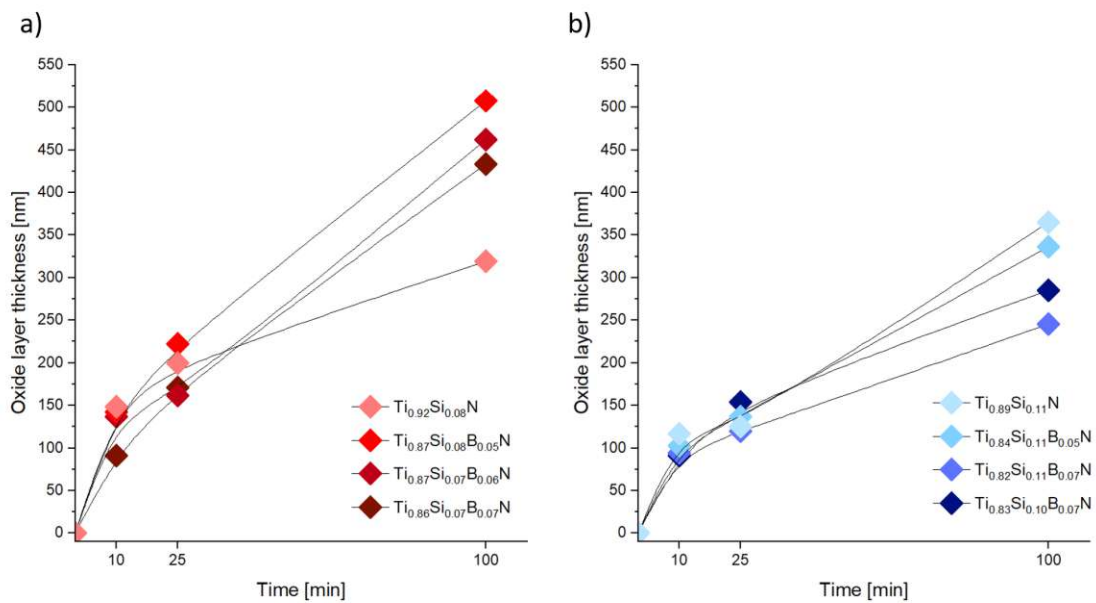


**Fig. 6.23:** Evolution of the oxide layers over time for a) 10 at.% Si and b) 15 at.% Si within the Ti/TiSi<sub>2</sub> target

These findings follow literature data suggesting that alloying Si to the binary TiN system substantially improves the oxidation resistance by forming SiO<sub>2</sub> protecting the TiN crystallites or due to the dense a-Si<sub>3</sub>N<sub>4</sub> phase preventing oxygen diffusion along the grain boundaries [39, 40, 81]. On the contrary, alloying boron to the ternary system degrades the oxidation resistance, as evidenced in Figure 6.23a, resulting from the lower oxidation resistance of BN compared to Si<sub>3</sub>N<sub>4</sub>. The poor oxidation resistance of BN is caused by a loss of boron due to oxidation and evaporation of BO<sub>x</sub> suboxides [7].

Particularly noteworthy is that the least boron-containing coatings are slightly less oxide-resistant than the films associated with higher B shares.

However, a more detailed analysis of Figure 6.23b shows that the ternary coating system (Ti<sub>0.89</sub>Si<sub>0.11</sub>N) develops a thicker oxide layer (365 nm after 100 min) over time than the quaternary system (245 nm for Ti<sub>0.82</sub>Si<sub>0.11</sub>B<sub>0.07</sub>N and 337 nm for Ti<sub>0.84</sub>Si<sub>0.11</sub>B<sub>0.05</sub>N). This implies that alloying boron to the Ti-Si-N films improves the oxidation resistance of the films.

The FIB images in Figure 6.24 compare the layer evolution for Ti<sub>0.92</sub>Si<sub>0.08</sub>N (Figure 6.24a) and Ti<sub>0.87</sub>Si<sub>0.07</sub>B<sub>0.06</sub>N (Figure 6.24b), after annealing at 800 °C for 100 min.



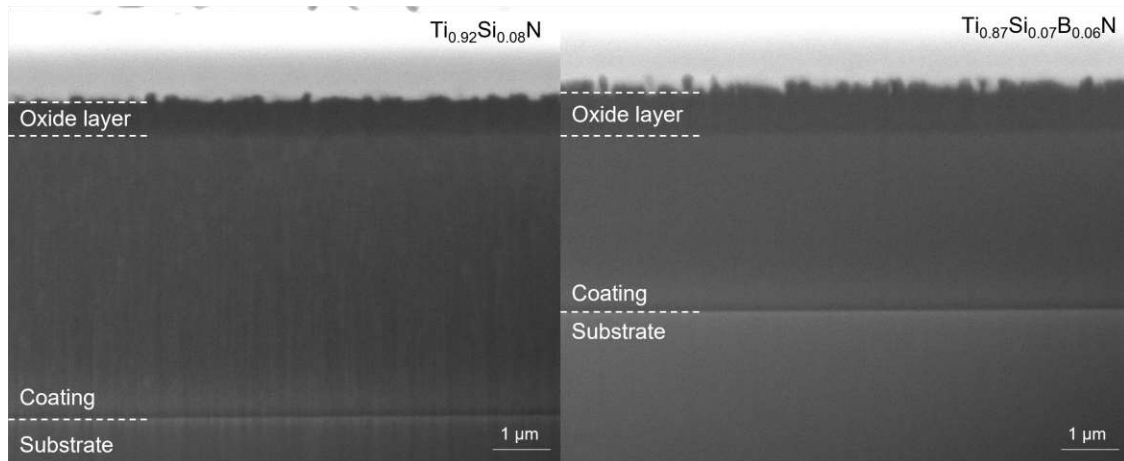


**Fig. 6.24:** Oxide layer thickness for (a)  $Ti_{0.92}Si_{0.08}N$  and (b)  $Ti_{0.87}Si_{0.07}B_{0.06}N$  coatings after 100 min at 800 °C

Both images show a well-defined interface between the coating and the developed oxide layer. However, due to the lower oxidation resistance of the BN phase,  $Ti_{0.87}Si_{0.07}B_{0.06}N$  (Figure 6.24b) demonstrates a thicker oxide layer of 433.7 nm compared to 319.5 nm for  $Ti_{0.92}Si_{0.08}N$  (Figure 6.24a).

## Conclusion

In summary, this study aimed to preserve the excellent mechanical properties of the well-researched Ti-Si-N coating system, while improving the tribological behavior by alloying boron to the ternary system.

In the first step, four Ti/TiSi<sub>2</sub> targets with different silicon contents (Ti<sub>1-x</sub>Si<sub>x</sub> with x = 10 at.%- 25 at.%) have been reactively sputtered to optimize the deposition parameters. In accordance to literature, the mechanical properties – in detail hardness – peaks out at a Si content of around 11 at.% before a decrease through a predominant formation of the Si<sub>3</sub>N<sub>4</sub> phase sets in. The SEM cross-section images clearly depict the evolution of the nanocomposite morphology, with decreasing TiN crystallite size embedded in an amorphous Si<sub>3</sub>N<sub>4</sub> matrix. The reduction of the columnar/crystallite size was also reflected by X-ray diffraction analysis. These results narrowed the target selection to two Ti/TiSi<sub>2</sub> targets containing a silicon content of 10 at.% and 15 at.% for further analysis. Detailed investigations have been carried out for co-sputtered Ti/TiSi<sub>2</sub> (at 1.25 A target current) and TiB<sub>2</sub> with varying currents between 0.25 A, 0.5 A, and 0.75 A to increase the share of boron content within the coatings.

Superior mechanical properties have been recorded for coatings deposited from the Ti/TiSi<sub>2</sub> target with 10 at.% Si reaching a maximum hardness of 36.5±1.49 GPa and a Young's modulus of 359.2±13.29 GPa at a boron content of 5.32 at.% (0.25 A). Due to the minor share of boron in the Ti-Si-B-N coatings, ranging between 5.32 at.% and 7.01 at.%, boron most probably exists in an amorphous BN phase surrounded by the TiN nano-crystallites, as examined by XRD and XRF analysis and reflected by SEM cross-sections. The soft a-BN phase is responsible for the decrease in hardness for coatings containing more than 5.3 at.% boron and a simultaneous decrease in silicon content. On the other hand, it was demonstrated that an increasing share of BN, leading to a reduced Young's modulus, promotes a low coefficient of friction, dropping to 0.78 and 0.83 for Ti-Si-B-N coatings, with 10 at.% and 15 at.% Si within the Ti/TiSi<sub>2</sub> targets, respectively. Particularly noteworthy is that the most significant decline in the COF was measured between approximately 5.3 at.% and 6.6 at.% boron for these Ti/TiSi<sub>2</sub> targets.

While the tribological properties benefited from alloying with boron to the coating system, the oxidation resistance suffers, resulting in faster-growing oxide layers due to the low oxidation stability of the may formed BN phase. Furthermore, the addition of B leads to a small reduction of Si influencing the diffusion mechanism to form SiO<sub>2</sub> rich oxide scales. The Ti-Si-B-N coatings sputtered from the Ti/TiSi<sub>2</sub> target with 10 at.% Si are less resistant against oxidation obtaining oxide scale thickness between 433.7 nm and 507.8 nm (Ti<sub>0.86</sub>Si<sub>0.07</sub>B<sub>0.07</sub>N and Ti<sub>0.87</sub>Si<sub>0.08</sub>B<sub>0.05</sub>N), while the coatings with high Si content developed a minimum oxide layer thickness of 336.7 nm after 100 min (Ti<sub>0.92</sub>Si<sub>0.08</sub>N).

Combining the individual results lead to the conclusion that alloying small amounts of boron to the Ti-Si-N coating system considerably improves the tribological properties by a further refinement microstructure accompanied by a suspected amorphous BN phase formation keeping the mechanical properties at a high level.

---

## Bibliography

- [1] T. Komiyama, E. Shamoto, I. Onozato, and K. Akazawa, *Precision Engineering* **72**, 613 (2021).
- [2] P. H. Mayrhofer, “Surface Technology,” (2022).
- [3] D. V. Shtansky, A. N. Sheveiko, M. I. Petrzhik, F. V. Kiryukhantsev-Korneev, E. A. Levashov, A. Leyland, A. L. Yerokhin, and A. Matthews, *Surface and Coatings Technology* **200**, 208 (2005).
- [4] D. V. Shtansky, E. A. Levashov, A. N. Sheveiko, and J. J. Moore2, “The Structure and Properties of Ti-B-N, Ti-Si-B-N, Ti-Si-C-N, and Ti-Al-C-N Coatings Deposited by Magnetron Sputtering Using Composite Targets Produced by Self-Propagating High-Temperature Synthesis (SHS),” *Tech. Rep.* 1 (1998).
- [5] E. A. Levashov and D. V. Shtansky, *Russian Chemical Reviews* **76**, 463 (2007).
- [6] S. Vepřek, M. Haussmann, and S. Reiprich, *Journal of Vacuum Science & Technology A: Vacuum, Surfaces, and Films* **14**, 46 (1996).
- [7] P. Karvánková, M. G. Vepřek-Heijman, M. F. Zawrah, and S. Vepřek, *Thin Solid Films* **467**, 133 (2004).
- [8] P. V. Kiryukhantsev-Korneev, D. V. Shtansky, M. I. Petrzhik, E. A. Levashov, and B. N. Mavrin, *Surface and Coatings Technology* **201**, 6143 (2007).
- [9] A. Fabrizi, R. Cecchini, P. V. Kiryukhantsev-Korneev, A. N. Sheveyko, S. Spigarelli, and M. Cabibbo, *Protection of Metals and Physical Chemistry of Surfaces* **53**, 452 (2017).
- [10] D. V. Shtansky, E. A. Levashov, A. N. Sheveiko, and J. J. Moore2, “Optimization of PVD Parameters for the Deposition of Ultrahard Ti-Si-B-N Coatings,” *Tech. Rep.* 3 (1999).
- [11] R. Boyer, G. Welsch, and E. W. Collings, eng*Materials properties handbook : titanium alloys*, 1st ed. (ASM International, Metals Park, OH, 1994).

- [12] E. Rolinski, ASM Handbook, Volume 4E, Heat Treating of Nonferrous Alloys **4E**, 604 (1984).
- [13] R. Ferro and A. Saccone, eng *Intermetallic chemistry*, 1st ed., Pergamon materials series (Pergamon, Elsevier, Amsterdam [u.a.], 2008).
- [14] H. Skulev, B. Drenchev, T. Mechkarova, L. Drenchev, and A. A. Balevski, “Kinetics of Surface Layers Growth in Gas Nitriding Ti-6Al-4V by Indirect Plasma Torch,” Tech. Rep. 2 (2014).
- [15] American Society for Metals, (1994).
- [16] J.-E. Sundgren, “Review Paper STRUCTURE AND PROPERTIES OF TiN COATINGS\*,” Tech. Rep. (1985).
- [17] S. T. Oyama, eng *The chemistry of transition metal carbides and nitrides*, 1st ed. (Blackie Academic & Professional, London [u.a.], 1996).
- [18] J. Sarkar, eng *Sputtering materials for VLSI and thin film devices*, 1st ed. (Elsevier, Amsterdam [u.a.], 2014).
- [19] Khidirov, Russian journal of inorganic chemistry. **56**, 298 (2011).
- [20] Lengauer, Journal of alloys and compounds an interdisciplinary journal of materials science and solid-state chemistry and physics **186**, 293 (1992).
- [21] H. Okamoto, “N-Ti (Nitrogen-titanium),” (2013).
- [22] S. Sambasivana and W. T. Petuskey, “Phase chemistry in the Ti-Si-N system: Thermochemical review with phase stability diagrams,” Tech. Rep. (1994).
- [23] Y. Yang, H. Lu, C. Yu, and J. M. Chen, Journal of Alloys and Compounds **485**, 542 (2009).
- [24] X. Ma, C. Li, and W. Zhang, Journal of Alloys and Compounds **394**, 138 (2005).
- [25] R. Hauert and J. Patscheider, “From alloying to nanocomposites - Improved performance of hard coatings,” (2000).
- [26] M. Paulasto, J. K. Kivilahti, and F. J. Van Loo, Journal of Applied Physics **77**, 4412 (1995).
- [27] R. Beyers, R. Sinclair, and M. E. Thomas, Journal of Vacuum Science and Technology B: Microelectronics and Nanometer Structures **2**, 781 (1984).

- [28] W. J. J. Wakelkamp, *Diffusion and phase relations in the systems Ti-Si-C and Ti-Si-N*, Ph.D. thesis (1991).
- [29] P. Rogl and J. Schuster, in *ASM International* (1992).
- [30] S. Vepřek, S. Reiprich, and L. Shizhi, *Applied Physics Letters*, 2640 (1995).
- [31] L. Shizhi, S. Yulong, and P. Hongrui, “Ti-Si-N Films Prepared by Plasma-Enhanced Chemical Vapor Deposition,” *Tech. Rep. 3* (1992).
- [32] F. Vaz, L. Rebouta, S. Ramos, M. F. Da Silva, and J. C. Soares, “Physical, structural and mechanical characterization of Ti Si N films 12x x y a a,” *Tech. Rep.* (1998).
- [33] M. Diserens, J. Patscheider, and F. Levy, “Improving the properties of titanium nitride by incorporation of silicon,” *Tech. Rep.* (1998).
- [34] S. Carvalho, E. Ribeiro, L. Rebouta, J. Pacaud, P. Goudeau, P. O. Renault, J. P. Rivière, and C. J. Tavares, *Surface and Coatings Technology* **172**, 109 (2003).
- [35] S. Vepřek, M. Hausmann, S. Reiprich, L. Shizhi, and J. Dian, *Surface and Coatings Technology* **86-87**, 394 (1996).
- [36] S. K. Mishra, “Toughening of nanocomposite hard coatings,” (2020).
- [37] P. H. Mayrhofer, C. Mitterer, and H. Clemens, *Advanced Engineering Materials* **7**, 1071 (2005).
- [38] Y. H. Cheng, T. Browne, B. Heckerman, P. Gannon, J. C. Jiang, E. I. Meletis, C. Bowman, and V. Gorokhovskiy, *Journal of Physics D: Applied Physics* **42** (2009).
- [39] J. B. Choi, K. Cho, M. H. Lee, and K. H. Kim, in *Thin Solid Films*, Vol. 447-448 (2004) pp. 365–370.
- [40] S. Vepřek, M. G. Vepřek-Heijman, P. Karvankova, and J. Prochazka, “Different approaches to superhard coatings and nanocomposites,” (2005).
- [41] Z. J. Liu, Y. H. Lu, and Y. G. Shen, *Journal of Materials Research* **21**, 82 (2006).
- [42] P. H. Mayrhofer and M. Stoiber, *Surface and Coatings Technology* **201**, 6148 (2007).
- [43] I. Asempah, J. Xu, L. Yu, H. Ju, F. Wu, and H. Luo, *Surface Engineering* **35**, 701 (2019).
- [44] W. Gissler, “Structure and properties of Ti-B-N coatings,” *Tech. Rep.* (1994).
- [45] Nowotny, *Monatshefte für Chemie Chemical monthly.* **92**, 403 (1961).

- [46] F. Kunc, J. Musil, P. H. Mayrhofer, and C. Mitterer, *Surface and Coatings Technology* **174**, 744 (2003).
- [47] M. Berger, M. Larsson, and S. Hogmark, “Evaluation of magnetron-sputtered TiB<sub>2</sub> intended for tribological applications,” Tech. Rep. (2000).
- [48] S. C. D. S. PalDey and S. C. Deevi, *Materials Science and Engineering: A* **342**, 58 (2003).
- [49] W. D. Westwood, *MRS Bulletin* **13**, 46 (1988).
- [50] D. M. Mattox, *Handbook of physical vapor deposition (PVD) processing* (William Andrew, 2010).
- [51] S. Berg and T. Nyberg, “Fundamental understanding and modeling of reactive sputtering processes,” (2005).
- [52] P. K. S. Sree Harsha, eng*Principles of Vapor Deposition of Thin Films* (Elsevier Science & Technology, Oxford, 2005).
- [53] G. H. Gilmer, H. Huang, and C. Roland, *Computational Materials Science* **12**, 354 (1998).
- [54] J. A. Thornton, “HIGH RATE THICK FILM GROWTH,” Tech. Rep. (1977).
- [55] A. Anders, *Thin Solid Films* **518**, 4087 (2010).
- [56] A. C. Fischer-Cripps, “Critical review of analysis and interpretation of nanoindentation test data,” (2006).
- [57] G. M. Pharr and W. C. Oliver, *MRS Bulletin* , 28 (1992).
- [58] M. Ermrich and D. Opper, *XRD for the analyst : getting acquainted with the principles* (2011).
- [59] A. A. Bunaciu, E. g. Udriștioiu, and H. Y. Aboul-Enein, “X-Ray Diffraction: Instrumentation and Applications,” (2015).
- [60] M. Birkholz, P. F. Fewster, and C. Genzel, eng*Thin film analysis by X-ray scattering* (Wiley-VCH, Weinheim, 2006).
- [61] L. D. Whittig and W. R. Allardice, in *Methods of Soil Analysis*, Vol. 5 (John Wiley & Sons, Inc, 1986) pp. 331–362.
- [62] R. Dinnebier and S. J. Billinge, in *Powder Diffraction: Theory and Practice* (2008) Chap. 1, pp. 1–19.

- [63] R. Jenkins, eng *X-ray fluorescence spectrometry*, A Wiley-Interscience publication (Wiley, New York [u.a.], 1988).
- [64] B. Beckhoff, eng *Handbook of practical X-ray fluorescence analysis : with 53 tables* (Springer, Berlin [u.a.], 2006).
- [65] Vrieling, *Thin solid films international journal on the science and technology of condensed matter films* **520**, 1740 (2012).
- [66] L. Page, eng *Encyclopedia of scanning electron microscopy* (NY Research Press, New York, 2015).
- [67] eng *ASM handbook : 8. Mechanical testing and evaluation*, 1st ed. (ASM International, Materials Park, Ohio, 2000).
- [68] eng *ASM handbook : 10. Materials characterization*, 3rd ed. (ASM International, Materials Park, Ohio, 1992).
- [69] R. Egerton, eng *Physical principles of electron microscopy : an introduction to TEM, SEM and AEM*, second edition. ed. (Springer, [Cham], 2016).
- [70] B. J. Inkson, in *Materials Characterization Using Nondestructive Evaluation (NDE) Methods* (Elsevier Inc., 2016) pp. 17–43.
- [71] J. I. Goldstein, eng *Scanning electron microscopy and x-ray microanalysis*, 3rd ed. (Kluwer Academic, Plenum Publ., New York, NY [u.a.], 2003).
- [72] H. Riedl-Tragenreif (2021).
- [73] R. Novak and T. Polcar, *Tribology International* **74**, 154 (2014).
- [74] R. P. Nair, D. Griffin, and N. X. Randall, *Wear* **267**, 823 (2009).
- [75] M. J. M. J. Neale and M. G. Gee, eng *Guide to wear problems and testing for industry* (William Andrew Pub., Norwich, N.Y., 2001).
- [76] F. Blateyron, in eng *Optical Measurement of Surface Topography* (Springer, Berlin [u.a.], 2011) pp. 71–106.
- [77] M. Bartosik, R. Hahn, Z. L. Zhang, I. Ivanov, M. Arndt, P. Polcik, and P. H. Mayrhofer, *International Journal of Refractory Metals and Hard Materials* **72**, 78 (2018).
- [78] G. Abadias, *Surface and Coatings Technology* **202**, 2223 (2008).
- [79] C. Ducros, V. Benevent, P. Juliet, and F. Sanchette, *Surface and Coatings Technology* **163-164**, 641 (2003).



- [80] G. Taghavi Pourian Azar and M. Ürgen, *Surface Engineering* **36**, 13 (2020).
- [81] M. Arab Pour Yazdi, F. Lomello, J. Wang, F. Sanchette, Z. Dong, T. White, Y. Wouters, F. Schuster, and A. Billard, *Vacuum* **109**, 43 (2014).
- [82] S. Hyun Kim, J. Kuk Kim, and K. Ho Kim, “Influence of deposition conditions on the microstructure and mechanical properties of Ti-Si-N films by DC reactive magnetron sputtering,” *Tech. Rep.* (2002).
- [83] Z. T. Yang, B. Yang, L. P. Guo, and D. J. Fu, *Journal of Alloys and Compounds* **473**, 437 (2009).
- [84] J. Patscheider, T. Zehnder, and M. Diserens, “Structure-performance relations in nanocomposite coatings,” *Tech. Rep.* (2001).
- [85] S. Veprek and S. Reiprich, “A concept for the design of novel superhard coatings,” *Tech. Rep.* (1995).
- [86] R. Hahn, A. Tymoszuk, T. Wojcik, A. Kirnbauer, T. Kozák, J. Čapek, M. Sauer, A. Foelske, O. Hunold, P. Polcik, P. H. Mayrhofer, and H. Riedl, *Surface and Coatings Technology* **420** (2021).
- [87] S. M. Yang, Y. Y. Chang, D. Y. Wang, D. Y. Lin, and W. T. Wu, *Journal of Alloys and Compounds* **440**, 375 (2007).
- [88] F. V. Kiryukhantsev-Korneev, M. I. Petrzhik, A. N. Sheveiko, E. A. Levashov, and D. V. Shtanskii, *Physics of Metals and Metallography* **104**, 167 (2007).
- [89] H. Bu, H. Zheng, H. Zhou, H. Zhang, Z. Yang, Z. Liu, H. Wang, and Q. Xu, *RSC Advances* **9**, 2657 (2019).